

Determining the observer's velocity using radio continuum surveys



A thesis submitted in partial fulfilment of the requirements for the degree of Magister Scientiae in the Department of physics and astronomy, University of the Western Cape.

Student: Nandrianina Randriamiarinarivo
E-mail: nandrianiana@gmail.com

Supervisor: Roy Maartens

Co-supervisor: Carlos Bengaly

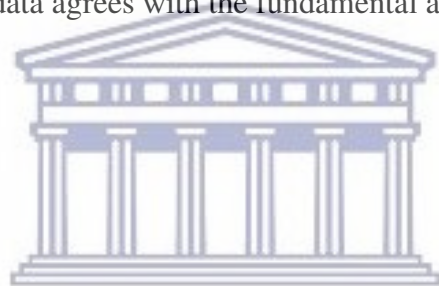


UNIVERSITY *of the*
WESTERN CAPE

Abstract

In the standard ('concordance') model of Cosmology, there is a fundamental assumption that the Universe is statistically isotropic and homogeneous on large scales, known as the Cosmological Principle. The Cosmological Principle requires that the dipole anisotropy apparent in the CMB should also be observed in galaxy number counts if this signal occurs due to the aberration and Doppler effects from our peculiar motion. This thesis will investigate the accuracy with which the cosmic kinematic dipole can be determined by comparing real data from NRAO VLA Sky Survey (NVSS) catalog with the simulated sky maps following its specifications. The mock maps are generated using FLASK code which assumes a lognormal distribution for the radio count density field from $z=0$ to $z=4$ and taking as an entry an angular power spectrum from CAMB which assumed a flat Λ CDM cosmology and a redshift distribution. After analysing the kinematic dipole, we turn to the analysis of statistical isotropy in the catalog. We used ANalysis Of Variance (ANOVA) test on patches in the sky of different radii as one of the statistical tools for the analysis. We found that as we go to a higher radius for the patches, we have a better agreement between the theory and the observation as expected. We also saw that the more we are rigorous on the rejection criteria, the smaller is the discrepancy between the observed and simulated number count distribution in the sky. We found an optimum choice of 25° as patch size, and if the accepted patches have a maximum of 30% of their pixels masked.

Therefore, we find that the NVSS data agrees with the fundamental assumption of statistical isotropy at angular scales $> 20^\circ$.



UNIVERSITY of the
WESTERN CAPE

Declaration

I declare that 'Determining the observer's velocity using radio continuum surveys' is my own work, that it has not been submitted before for any degree or examination in any other university, and that all the sources I have used or quoted have been indicated and acknowledged as complete references.

Nandrianina Randriamiarinarivo

13th March, 2019

Signed:



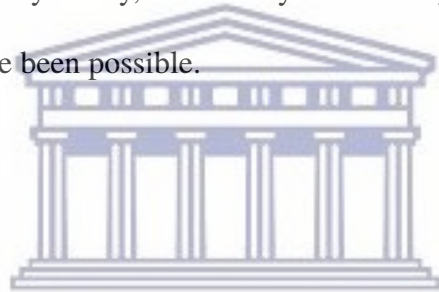
Acknowledgments

I would like to express my deepest appreciation and sincerity to my supervisor Prof. Roy Maartens and my co-supervisor Dr. Carlos Bengaly for their support and guidance for my Masters project, as well as my educational institute, University of Western Cape (UWC) and the Center of Radio Cosmology (CRC) team for giving me this amazing opportunity.

Secondly, I would like to thank the astro UWC group for their incredible hospitality and valuable advices about my Masters project and also for making my time during my Master very pleasant and educational.

Finally I would like to acknowledge my family, even if they are far away, for the uttermost encouragement.

Without you all, this would not have been possible.



UNIVERSITY of the
WESTERN CAPE

Contents

1	Introduction	1
2	Overview on Cosmology	2
1	Overview on radio astronomy	2
1.1	Radio galaxies	4
1.2	Radio continuum surveys	5
2	Standard model of Cosmology	7
2.1	Evolution of the Universe	10
2.1.1	Dynamics of the Universe	12
2.1.2	Structure formation	15
2.1.3	Eras of evolution	18
2.2	Cosmological distance	21
2.3	2-point correlation function and power spectrum	23
2.4	The kinematic dipole	26
3	Analysis procedures	30
1	Visualisation and simulation tools	30
1.1	HEALPix	30
1.2	FLASK	32
2	Procedure analysis technique	34
2.1	The NVSS survey	34
2.2	Testing the isotropy of the NVSS map	38
2.3	ANOVA-test	40
4	Results and discussions	42
1	F-statistic	42
2	Local variance	43
5	Conclusion	47
	Appendices	48
A	Useful Astronomical Units	49
B	Astronomical and Cosmological constants	50
C	Special functions	51
1	Legendre polynomials	51
2	Spherical Bessel function	51
3	Fourier tranforms	52

Introduction

The Universe has different kind of structures that formed and grew with the expansion of the Universe itself. Cosmology is a science that studies particularly the evolution and structure of the Universe in large scale. Scientists have succeeded to map the Universe from observations. The study of the cosmic microwave background (CMB) has brought amazing improvement in the field of Cosmology. From the analysis of the distribution of the temperature of this remnant radiation, we found evidence that the Universe is statistically homogeneous and isotropic which combined together comprise the so called Cosmological Principle (CP). Recently radio astronomers made a huge step in term of observation by planning much bigger survey such as the Square Kilometer Array (SKA) based in South Africa which cover an area $> 20,000deg^2$ [1].

Here, we will study the accuracy with which the cosmic kinematic dipole can be determined, by comparing real data to simulated sky maps using [2]. We will investigate also the standard model of Cosmology, especially the isotropy of the Universe. Indeed the CP implies that the kinematic dipole in the galaxy number count map should be consistent with that of the cosmic microwave background. Previous works studied this topic such as in [3] and [4] where they tested the cosmological isotropy with Gamma-Ray Bursts and Type Ia supernovae (SNe Ia) compilation independently. They reached the conclusion that there is no evidence for a significant anisotropy in the sky using these data.

In this work, we will investigate the dipole and isotropy of the Universe using a radio count map constructed from the NRAO VLA Sky Survey (NVSS) catalog [5], so we compare the observational data with the theory by means of simulated count maps assuming the LCDM matter power spectrum. Then we will compute the value of the expected kinematic dipole which we will compare also with the observation. We found good consistency between the observed and simulated anisotropies on the radio count map.

Overview on Cosmology

Radio Cosmology is the study of the origin and evolution of the Universe in the radio view of the electromagnetic spectrum. In fact, we can say that it is a combination of radio astronomy and observational Cosmology. So in this section, we will review some of the concepts used in this work, putting emphasis on radio astronomy concepts and Cosmology review.

1 Overview on radio astronomy

Radio astronomy studies astronomical phenomena that are often invisible or hidden in some part of the electromagnetic spectrum.

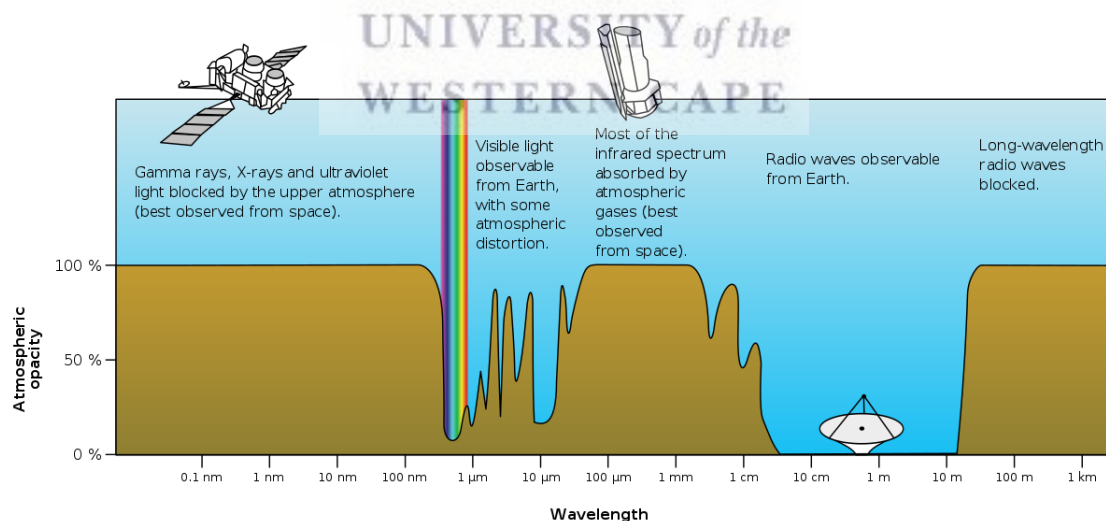


Figure 2.1: The opacity of the Earth atmosphere with respect to electromagnetic spectrum. Credit:https://commons.wikimedia.org/wiki/File:Atmospheric_electromagnetic_opacity.svg

As we can see in figure 2.1, most of the electromagnetic waves are blocked by the earth atmosphere

while in radio band, it is largely transparent. Radio band is subdivided according to their frequency or wavelength as we can see in figure 2.2.

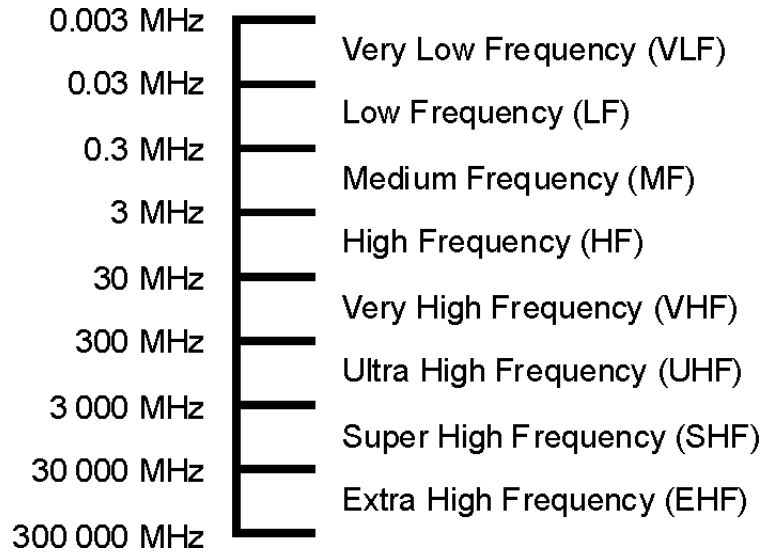
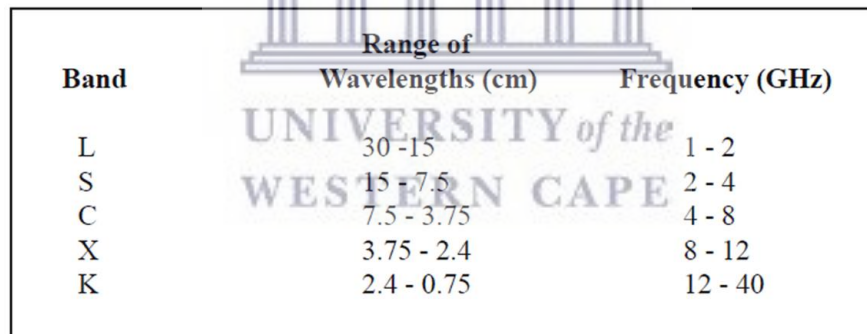


Figure 2.2: Radio frequency spectrum. Credit: <https://www.electronics-notes.com/articles/antennas-propagation>

However in radio astronomy, we often use different nomenclature of these radio frequency bands in radio astronomy, as summarized in figure 2.3.



Band	Range of Wavelengths (cm)	Frequency (GHz)
L	30 - 15	1 - 2
S	15 - 7.5	2 - 4
C	7.5 - 3.75	4 - 8
X	3.75 - 2.4	8 - 12
K	2.4 - 0.75	12 - 40

Figure 2.3: Radio bands. Credit: <https://www.mdsc.nasa.gov>

Unlike optical observation, we use an antenna to detect radio waves but how? The radio emission can be firstly classified in to two categories: thermal and non-thermal. The thermal emission is mainly due to the vibration of atoms and it only depends on the temperature of the sources. It is sometimes referred to as blackbody radiation in which the spectrum of the radiation can be fitted by the Planck's law which is defined by:

$$B_{\lambda}(T) = \frac{2hc^2}{\lambda^5} \frac{1}{\exp\left(\frac{hc}{kT\lambda}\right) - 1} \quad (2.1)$$

The nearest example of a source that produces such radiation is our sun. The most common example of non-thermal radiation is synchrotron radiation and the Compton scattering process. Synchrotron radiation is emitted when an electron or a charged particle spirals nearly at speed of light along magnetic field lines as illustrated in figure 2.4. In fact, such phenomena can be seen in quasars, pulsars, supernovae or in an active galaxy nuclei. It is easy to identify during observation since the synchrotron emission dominates the sky at low frequencies while the thermal radiation is more dominant in high frequencies.

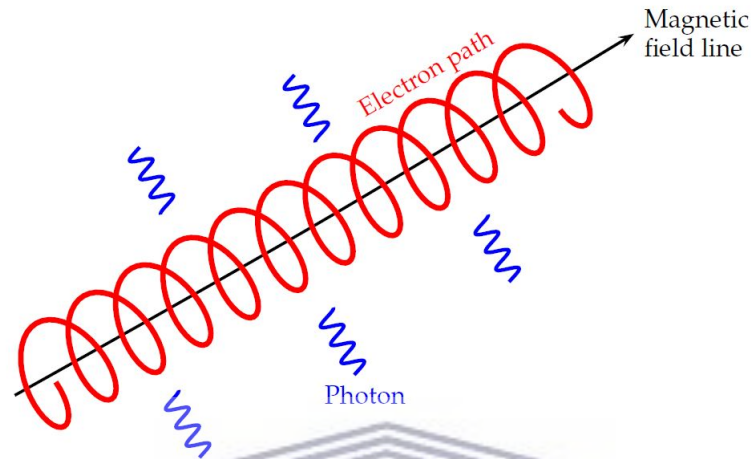


Figure 2.4: Mechanism of the synchrotron radiation. Credit: http://spiff.rit.edu/classes/ast613/lectures/radio_i/

In terms of observation, radio astronomers also use hydrogen atoms because of their spin-flip transition which emits radio photons of 21 cm wavelength or 1.42 GHz in the rest frame as we can see the illustration of the process in figure 2.5.

Indeed in radio astronomy, we tend to observe celestial objects which strongly emit in radio waves. Some of the most common observed radio sources especially in cosmology are the radio galaxies, pulsars and supernovae. In the next session, we will talk briefly about radio galaxies.

1.1 Radio galaxies

Radio astronomy can be defined as the study of the radio emissions from a given source in the vast Universe. However, most of the celestial objects emit radio waves but with different amounts of energy. Here in the following paragraph, we will focus on the most targeted kind of radio source.

Radio galaxies are among the most common used radio sources in astronomy. They are galaxies that emit strong radio waves more than the so-called normal galaxies. Indeed according to [6], we know that the radio luminosity of a radio galaxy is in the range of 10^{40} to 10^{45} erg/sec while a normal galaxy like the Milky Way is 10^{38} to 10^{40} erg/sec. In terms of structure, radio galaxies have three components in general: core, jets and the two lobes. We measure the radio emission from the galaxy using radio telescopes and study it afterwards. It is part of what is called as Double Radio Sources Associated with Galactic Nuclei or DRAGN. These are large-scale radio sources that are produced by oppositely directed jet outflows.

From [7], we know that the most distant radio galaxy detected now is at redshift $z = 5.72$, which is near

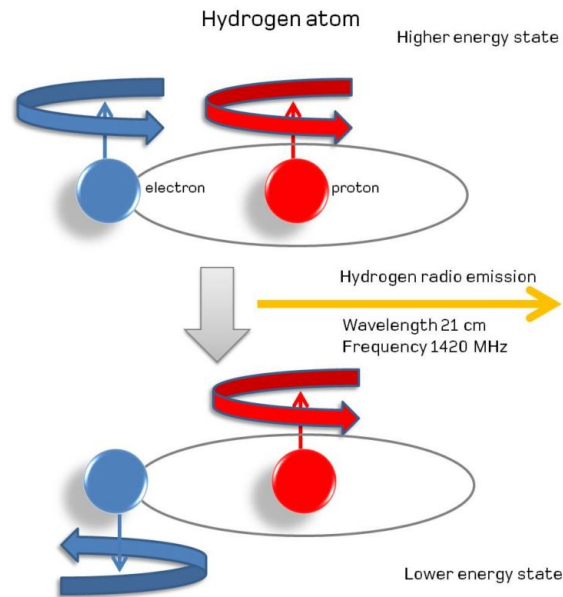


Figure 2.5: Emission of the radio signal at 21cm from an excited hydrogen. Credit: <https://www.skatelescope.org/>

to the end of the re-ionization era, observed by the TIFR GMRT Sky Survey (TGSS) at 150 MHz. In astronomy, depending on what we want to measure, we have different types of survey. However the one that we will use here is what we called radio continuum survey. We will discuss about it in the next section.

1.2 Radio continuum surveys

In radio astronomy, we use radio telescope, which we can see in figure 2.6 the latest design used for the MeerKAT project to detect and receive radio signal from a given source or phenomena. Nowadays, we use the well known interferometry technique which consists of multiple radio antenna connected to each other.

Interferometry technique consists of combining data from multiple single dish telescopes by taking into account the delay τ_g in which the signal (V_i) is received by the individual antenna. One of major advantages of the interferometers is the resolution. Indeed we can have a much better resolution compared to the single dish telescope since it is no longer limited by the diameter of the telescope but instead it depends on the baseline b , of the interferometry, which can be defined as the distance between two antennas in the observation site.

Radio continuum surveys collect the total emission from radio galaxies, which is dominated by synchrotron radiation. Unlike the 21cm line emission, synchrotron radiation has no spectral feature and therefore radio continuum surveys do not measure the redshift of sources. However, since radio galaxies are very bright, radio continuum surveys can reach very high redshifts.

Radio continuum surveys give a radio map of the sky by looking at the distributions of radio sources intensity. The radio continuum surveys can be used to study galaxy evolution and Cosmology, to name a few examples. They provide also a totally different view compared to other observations in different wavelengths, allowing deeper and more accurate science of some astrophysical phenomena. Therefore, radio continuum survey can be done using single dish or by interferometer by measuring the flux density



Figure 2.6: Single dish radio telescope designed for MeerKAT. Credit: <https://en.wikipedia.org/wiki/MeerKAT>

from a targeted radio source. Flux density can be defined by:

$$S_\nu \approx \int_{source} I_\nu(\theta, \phi) d\Omega, \tag{2.2}$$

for a small angle in which $I_\nu(\theta, \phi)$ and $d\Omega$ are the specific intensity in term of the coordinate of the sources and the solid angle subtended by the latter. However we can express also the flux density of an isotropic radiating source by:

$$S_\nu = \frac{L_\nu}{4\pi r^2} \tag{2.3}$$

where L_ν is the spectral luminosity and r is the distance of the source.

The NVSS is one of the largest radio survey. It has a good sensitivity and angular resolution where we can see the specifications in table 2.1.

Name	Area (deg^2)	θ (arcsec)	ν (GHz)	σ_n ($\mu Jy/\Omega_b$)
NVSS	3.4×10^4	45	1.4	450

Table 2.1: Specification of the NVSS at 1.4GHz. from [8]

It also includes a different type of sky survey which includes: the Faint Images of Radio Sky at Twenty-centimeters or FIRST survey.

In figure 2.7, we have all the other major radio continuum survey in which we can see their evolutions in terms of coverage area and also their precision of point source detection.

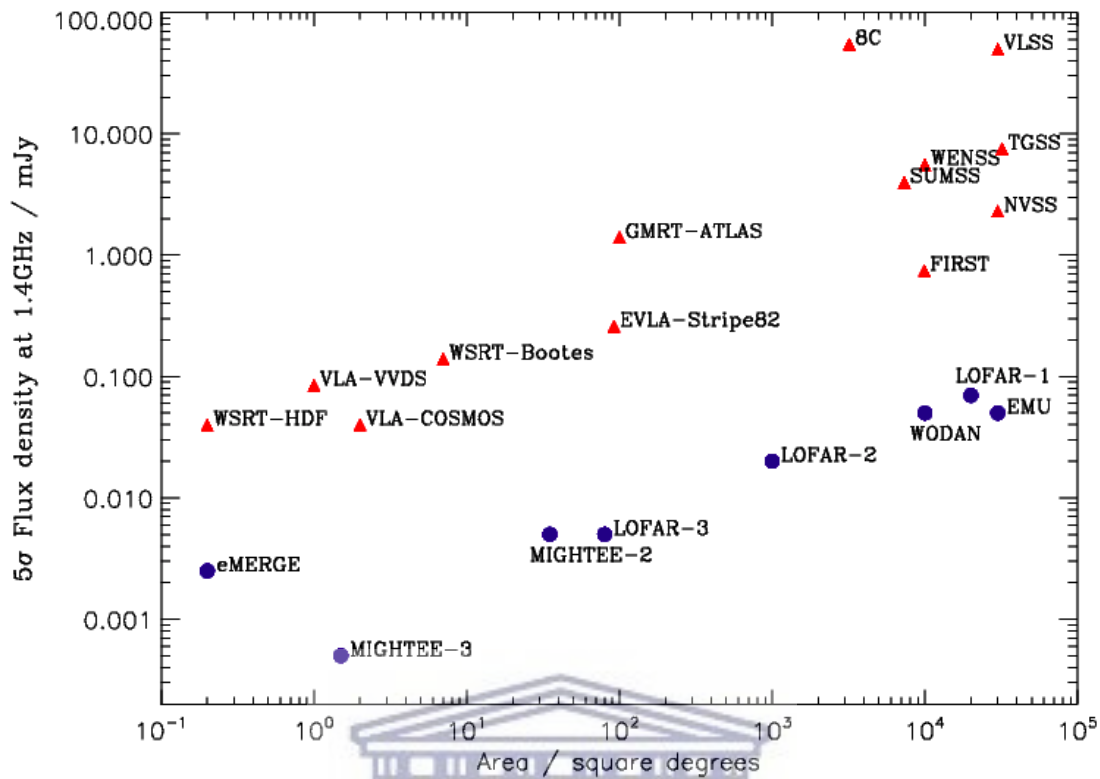


Figure 2.7: Sensitivity of radio continuum surveys with respect to the sky coverage of the surveys. Credit: [9]

2 Standard model of Cosmology

We assume homogeneity and isotropy of the Universe, on sufficiently large scale, is called as ‘Cosmological Principle’. Isotropy means that the Universe looks nearly the same at every direction around a fundamental observer and homogeneity means that fundamental observers at different regions of the Universe would see roughly the same Universe. We will call fundamental observers those which the only anisotropy seen in the Universe is due to the peculiar velocity, hence manifested dipole anisotropy in cosmic observations [10]. Therefore, if all fundamental observers see a statistically isotropic Universe, this leads to statistical homogeneity. We can see the illustration of these two concepts in figure 2.8. On small scales, the Universe is rather inhomogeneous and clumpy, but on large scales, galaxy surveys have been showing that the Universe is consistent with statistical homogeneous.

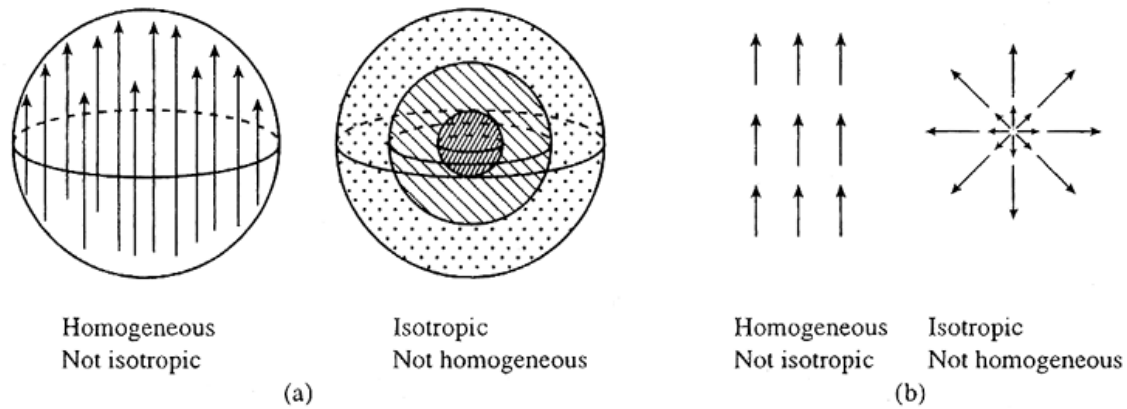


Figure 2.8: Illustration the concept of homogeneity and isotropy in three dimensional (a) and in two dimensional (b). Credit: [11]

The 'Copernican principle' states that there is no special place in the Universe. In fact if we associate this principle with the isotropical aspect of the Universe so at every point in the Universe everything looks the same in all direction. Indeed this will lead to a homogeneous Universe and thus the affirmation of the Cosmological Principle. In [12], they study the Copernican principle by assuming spatial inhomogeneity as an alternative to the dark energy.

In figure 2.9, we exhibit the sky maps of CMB temperature fluctuations as seen from different satellites. Even in early missions, like COBE, we could already note the small temperature fluctuations across the sky ($\Delta T \sim 10^{-5}$ K), thus providing a good probe of cosmic isotropy. Years later, we could probe these fluctuations with much higher resolution, confirming what has been found with COBE. Note, these maps are obtained after removing the monopole component ($T \approx 2.73$ K), and the dipole component ascribed to our motion relative to the CMB ($\Delta T \sim 3$ mK). Until now we did not find a significant anisotropy on large scale with all the observations we made like the CMB, galaxy distribution, the study of supernovae Ia and others assuming a given cosmological model. For the homogeneity, the best we can do is to test the consistency with it since we can only observe on the light-cone not within (figure 2.10).

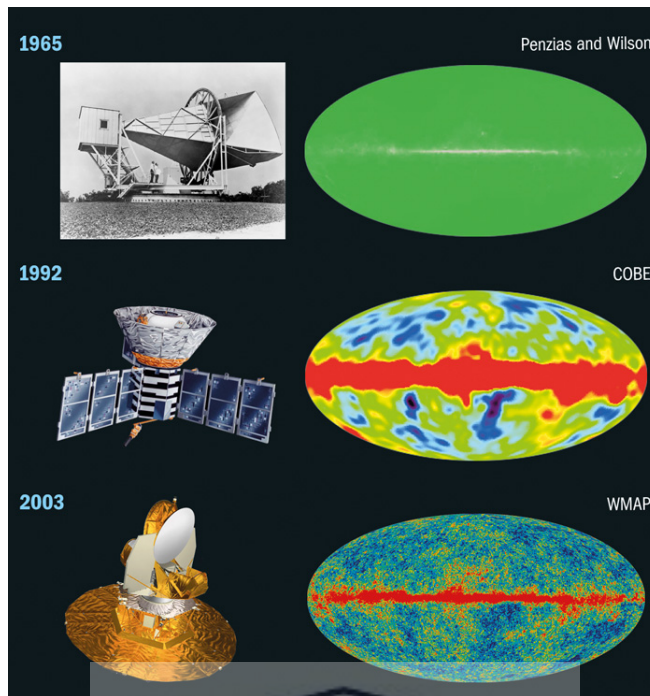


Figure 2.9: Sky temperature map observed since the early time of Penzias and Wilson in 1965 to the era of WMAP in 2003. Credit: <https://physicsworld.com/>

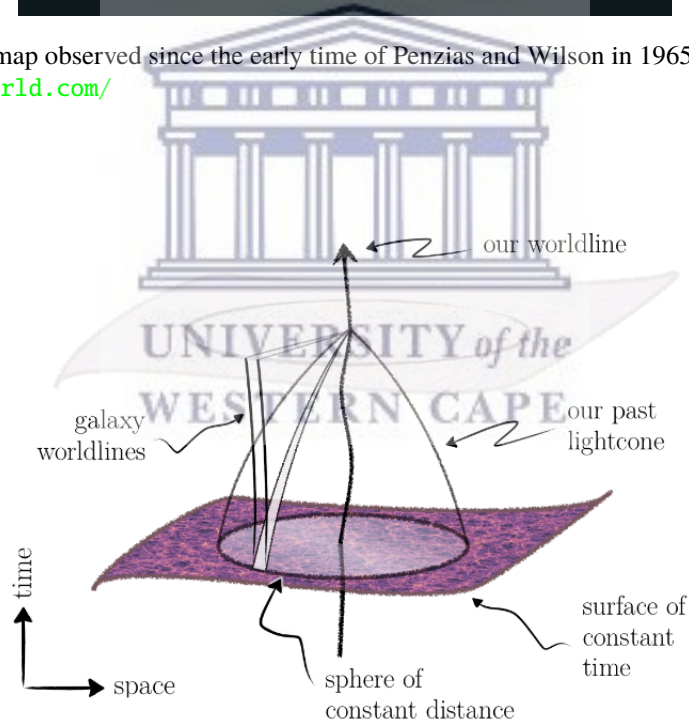


Figure 2.10: Our past lightcone. Credit : [12]

2.1 Evolution of the Universe

We know from the last section that the Universe can be approximated as isotropic on large scale. We know since several years now that our Universe is expanding and accelerating.

Redshift is an observable quantity that we often use to describe and study the history of the Universe. It is the change in wavelength of a photon from a source in motion. In fact if a source (like galaxy) moves away from the observer, he or she would see it redshifted, and if it moves toward us then it is blueshifted. It is defined by:

$$z = \frac{\lambda_0 - \lambda_1}{\lambda_1} \quad (2.4)$$

where λ_0 represent the wavelength of photon from source observed at t_0 and λ_1 the wavelength emitted at t_1 which is a earlier time.

Redshift is the most used parameter in astronomy, since we can express all the other quantity as a function to this variable. In fact, the scale factor a can be expressed in term of the redshift as :

$$a(t) = \frac{1}{1 + z} \quad (2.5)$$

which only depends on time t due to the homogeneity assumption. In this expression, we normalized in the scale factor measured today as $a(t_0) = 1$. We have the following expression for a in term of time t :

$$a(t) = a(t_0)[1 + (t - t_0)H_0 + \dots] \quad (2.6)$$

H_0 is the the Hubble constant which represents the current expansion rate of the Universe as given by

$$H(t) = \frac{\dot{a}(t)}{a(t)} \quad (2.7)$$

We can also define the Hubble length d_H from this parameter

$$d_H = \frac{c}{H} \quad (2.8)$$

where c is the speed of light.

We need to define metric in order to study and understand the behavior of the Universe on large scales. As we discussed in previous sections, the Universe is approximately homogeneous and isotropic in large scale so we define a metric that satisfies the Cosmological Principle. The metric is called the Friedmann-Robertson-Walker (FRW) metric by adopting the - +++ convention:

$$ds^2 = -c^2 dt^2 + a^2(t) \left(\frac{dr^2}{1 - kr^2} + r^2(d\theta^2 + \sin^2 \theta d\phi^2) \right), \quad (2.9)$$

where k is the curvature parameter which we can see in figure 2.11. It determines the geometry of Universe. In fact, it can have three possible values and r , θ and ϕ are the spherical coordinates.

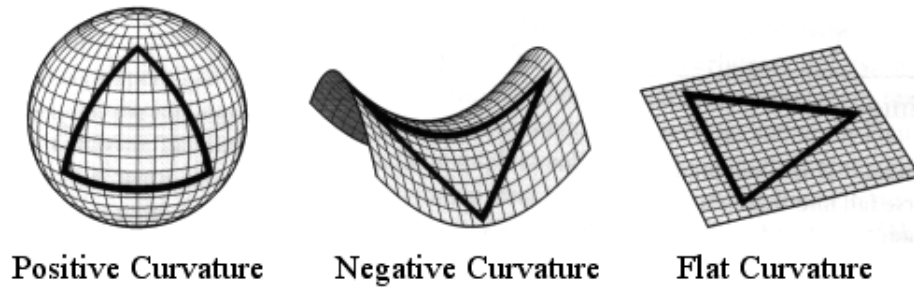


Figure 2.11: Three possibility type of geometry of the Universe depending on the value of k where $k = 1$: closed Universe, $k = -1$: open Universe, $k = 0$: Flat Universe. Credit: <http://abyss.uoregon.edu/~js/cosmo/>

By doing a coordinate transformation:

$$r_{phys} = a(t)r \tag{2.10}$$

to get the physical distance in which the physical velocity is given by:

$$v_{phys} = \frac{dr_{phys}}{dt} = v_p + Hr_{phys} \tag{2.11}$$

where we can see that it is a combination of the peculiar velocity v_p and the Hubble flow.

We can also rewrite the FRW metric in (2.33) as :

$$ds^2 = a^2(\tau) \left[-d\tau^2 + (d\chi^2 + F^2(\chi)(d\theta^2 + \sin^2 \theta d\Phi^2)) \right] \tag{2.12}$$

where $d\chi = \frac{dr}{1-kr}$ and we can define $F(\chi)$ as follow:

$$F^2(\chi) = \begin{cases} \sinh^2 \chi, & \text{if } k = -1 \\ \chi^2, & \text{if } k = 0 \\ \sin^2 \chi, & \text{if } k = 1 \end{cases} \tag{2.13}$$

and τ is the conformal time which can be defined as :

$$\tau = \int \frac{dt}{a(t)} \tag{2.14}$$

In equation (2.12), $ds = 0$ represents the null geodesic or also known as lightlike interval. Then we have $ds^2 < 0$ in which the interval is timelike and lastly $ds^2 > 0$ which represents a spacelike interval where we can see in figure 2.12 that the timelike geodesics are inside the light cone which is generated by the null geodesics.

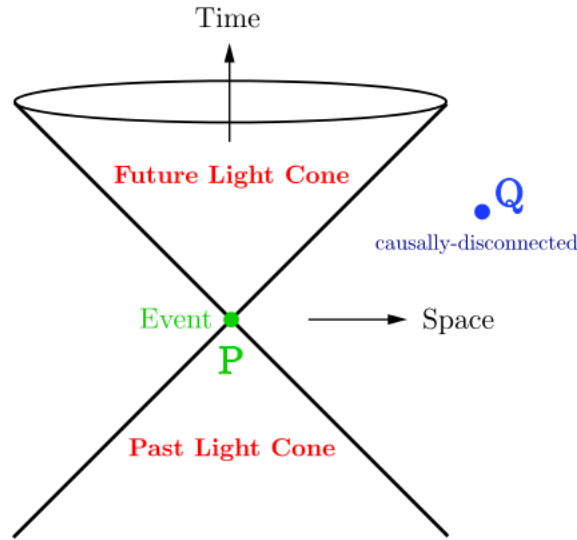


Figure 2.12: Representation of the light cone. Credit: [13]

2.1.1 Dynamics of the Universe

Now we will discuss more about the different epochs that happened throughout the evolution of our Universe since its beginning.

The scale factor $a(t)$ represents the size of our Universe compared to its current state so we need to understand the evolution of $a(t)$ with respect to time t . In fact we need the Einstein equations:

$$R_{\mu\nu} - \frac{1}{2}g_{\mu\nu}R = 8\pi GT_{\mu\nu} \tag{2.15}$$

where $R_{\mu\nu}$ and R are the Ricci tensor and the Ricci scalar and $g_{\mu\nu}$ is the metric tensor. $T_{\mu\nu}$ is the energy momentum tensor which follow the equation for perfect fluid:

$$T_{\mu\nu} = (\rho + p)u_{\mu}u_{\nu} + g_{\mu\nu}p \tag{2.16}$$

where ρ and p are the density and pressure of a fluid. By combining equations (2.15) and (2.16), we get the Friedmann equations:

$$H^2 = \left(\frac{\dot{a}}{a}\right)^2 = \frac{8\pi G}{3}\rho - \frac{k}{a^2} \tag{2.17}$$

$$\tag{2.18}$$

$$\dot{H} + H^2 = \frac{\ddot{a}}{a} = -\frac{4\pi G}{3}(\rho + 3p) \tag{2.19}$$

The energy momentum tensor is conserved which means that:

$$\nabla_{\mu}T^{\mu}_{\nu} = 0 \tag{2.20}$$

which yield the continuity equation:

$$\dot{\rho} + 3\frac{\dot{a}}{a}(\rho + p) = 0 \quad (2.21)$$

We can also write the pressure p in term of the density ρ such that:

$$p = \omega\rho, \quad (2.22)$$

So from those defined equations, we can solve for $a(t)$ with respect to the phase in which the expansion occurred. In the following relations, we can see the different solutions of the equations for different cases:

$$a(t) \propto \begin{cases} t^{2/3(1+\omega)}, & \text{if } \omega \neq -1 \\ e^{Ht}, & \text{if } \omega = -1 \end{cases} \quad (2.23)$$

In table 2.2, we show the matter dominated (MD), radiation dominated (RD) and dark energy dominated (DD) Universe for given value of ω .

Universe	ω	$a(t)$
MD	0	$t^{2/3}$
RD	$\frac{1}{3}$	$t^{1/2}$
DD	-1	e^{Ht}

Table 2.2: Evolution of the scale factor depending on the component that dominates the energy budget of the Universe.

These phases occurs at different periods during evolution of the Universe. The radiation dominated phase for example occurred during the early time in which photon are in thermal equilibrium with the relativistic species. Then we have the matter-radiation equality epoch where the density of matter and radiation are equal which can be translated as:

$$\rho_m(z_{eq}) = \rho_r(z_{eq}) \quad (2.24)$$

$$\rho_{m,0}(1 + z_{eq})^4 = \rho_{r,0}(1 + z_{eq})^3 \quad (2.25)$$

$$1 + z_{eq} = \frac{\rho_{r,0}}{\rho_{m,0}} \quad (2.26)$$

Later on, we have the recombination era where the electron and proton start binding together because the temperature was low enough. Since the electrons were captured by protons, the photons no longer interacted with baryons so the photons can freely travel and the Universe becomes transparent. We call this cosmic radiation as the Cosmic Microwave Background or CMB. Matter starts dominating the radiation and continues until the matter dark energy equality.

Let us define density parameter:

$$\Omega_i = \frac{\rho_i}{\rho_c} \quad (2.27)$$

where the subscript i represent the component of the Universe and ρ_c is the critical density defined by

$$\rho_c = \frac{3H^2}{8\pi G} \quad (2.28)$$

which indicates the limiting value of the density. If we have density lower than critical value then we have a spatially open Universe whereas if it is higher it is a spatially closed Universe.

So if we assume a flat Universe with matter and dark energy as component, the Friedmann equation become:

$$H^2 = H_0^2[\Omega_{m,0}(1+z)^3 + \Omega_{\Lambda,0}] \quad (2.29)$$

where the subscript 0 indicates the present time and Ω_{Λ} is the density parameter for dark energy which obeys also the following relation:

$$\Omega_m + \Omega_{\Lambda} = 1 \quad (2.30)$$

The solution of 2.29 is:

$$a(t) = \left(\frac{\Omega_{m,0}}{\Omega_{\Lambda,0}} \right)^{\frac{1}{3}} \sinh^{\frac{2}{3}} \left(\frac{3}{2} \sqrt{\Omega_{\Lambda,0}} H_0 t \right) \quad (2.31)$$

We can find the redshift of matter-dark energy equality like the matter-radiation equality one by equating the density of matter and the dark energy:

$$z_{eq} = \left(\frac{\Omega_{\Lambda,0}}{\Omega_{m,0}} \right)^{\frac{1}{3}} - 1 \quad (2.32)$$

Let just notice that Λ is the best candidate we have till now for the dark energy but of course there are other dark energy models.

2.1.2 Structure formation

During the epochs before the release of the cosmic microwave background, the Universe was really hot and the matter and photons are coupled. However after the decoupling era, structure start to form and grow. We know that there was a primordial fluctuation in density which can be one the causes of the anisotropy of the observed CMB temperature. In fact those perturbations under gravitational instabilities form the large scale structure that we know today. The Universe is mainly composed by: dark matter, baryons, photon and neutrino which are dominated by the dark energy. We will study the evolution of the gravitational potential and the density perturbation of dark matter and baryons. We use mainly the reference [13].

From here on, we will choose to work in conformal Newtonian Gauge in which the metric $g_{\mu\nu} = \bar{g}_{\mu\nu} + \delta g_{\mu\nu}$ is defined by

$$g_{\mu\nu} = a^2 \begin{bmatrix} -(1 + 2\Phi) & 0 & 0 & 0 \\ 0 & (1 - 2\Psi) & 0 & 0 \\ 0 & 0 & (1 - 2\Psi) & 0 \\ 0 & 0 & 0 & (1 - 2\Psi) \end{bmatrix} \quad (2.33)$$

where Φ and Ψ are scalar potentials however here we have $\Phi = \Psi$ since our anisotropic stress is zero. Notice also that $\bar{g}_{\mu\nu}$ is the unperturbed metric.

We can also define the perturbed Ricci tensor: $R_{\mu\nu} = \bar{R}_{\mu\nu} + \delta R_{\mu\nu}$ and so we got the perturbed component:

$$\begin{aligned} \delta R_{00} &= 3(\Phi'' + 2\mathcal{H}\Phi') + \Delta\Phi \\ \delta R_{0i} &= 2\partial_i(\Phi' + \mathcal{H}\Phi) \\ \delta R_{ij} &= [\nabla^2\Phi - \Phi'' - 6\mathcal{H}\Phi' - 4(\mathcal{H}' + 2\mathcal{H}^2)\Phi]\delta_{ij} \end{aligned} \quad (2.34)$$

where $\mathcal{H} = aH$ and using these Ricci tensor, we can define the Ricci scalar as $R = \bar{R} + \delta R$ such that:

$$R = g^{\mu\nu} R_{\mu\nu} = (\bar{g}^{\mu\nu} + \delta g^{\mu\nu})(\bar{R}_{\mu\nu} + \delta R_{\mu\nu}) \quad (2.35)$$

Hence:

$$\delta R = 2a^{-2}[\Delta\Phi - 3\Phi'' - 12\mathcal{H}\Phi' - 6(\mathcal{H}' + \mathcal{H}^2)\Phi] \quad (2.36)$$

For the case of the perturbed energy momentum tensor $T_{\mu\nu} = \bar{T}_{\mu\nu} + \delta T_{\mu\nu}$, using the definition in equation (2.16), we can express $\delta T_{\mu\nu}$ as:

$$\begin{aligned} \delta T_{00} &= a^2(\delta\rho + 2\bar{\rho}\Phi) \\ \delta T_{0i} &= -a^2(\bar{\rho} + \bar{p})\partial_i V \\ \delta T_{ij} &= a^2(\delta p - 2\bar{p}\Phi)\delta_{ij} \end{aligned} \quad (2.37)$$

where

$$v_i = \partial_i V \quad (2.38)$$

and the four-velocity is:

$$u^\mu = a^{-1}(1 - \Phi, v^i) \quad (2.39)$$

We can write the perturbed Einstein equation as:

$$\delta R_{\mu\nu} + \frac{1}{2}\bar{R}\delta g_{\mu\nu} + \frac{1}{2}\delta R\bar{g}_{\mu\nu} = 8\pi G\delta T_{\mu\nu} \quad (2.40)$$

So using equations (2.33), (2.34), (2.36) and (2.37) in equation (2.40), we got the following relations:

$$(00) : \nabla^2\Phi = 4\pi G a^2 \delta\rho + 3\mathcal{H}(\Phi' + \mathcal{H}\Phi) \quad (2.41)$$

$$(0i) : \Phi' + \mathcal{H}\phi = -4\pi G a^2 \bar{\rho}(1 + \omega)V \quad (2.42)$$

$$(ij) : \Phi'' + 3\mathcal{H}\Phi' + [4\mathcal{H}' + (2 + 3\omega)\mathcal{H}^2]\Phi = 4\pi G a^2 \delta p \quad (2.43)$$

In fact equation (2.43) can be also written as:

$$\Phi'' + 3(1 + C_s^2)\mathcal{H}\Phi' + 3\mathcal{H}^2\Phi + C_s^2 k^2\Phi = 0 \quad (2.44)$$

where we have:

$$C_s^2 = \frac{\delta\rho}{\delta p} = \frac{\bar{\rho}}{\bar{p}} \quad (2.45)$$

$$\nabla^2 = -k^2 \quad (2.46)$$

So the gravitational potential are governed by the Bardeen equation which we can see in equation (2.44).

For radiation dominated Universe which implies that $C_s^2 = \frac{1}{3}$, the differential equation in (2.44) become:

$$\Phi'' + \frac{4}{\eta}\Phi' + \frac{k^2}{3}\Phi = 0 \quad (2.47)$$

We can solve this equation analytically:

$$\Phi = 3\Phi_i \left(\frac{\sin(ky/\sqrt{3}) - (ky/\sqrt{3}) \cos(ky/\sqrt{3})}{(ky/\sqrt{3})^3} \right) \quad (2.48)$$

where $y = \frac{a}{a_{eq}}$ and a_{eq} is the scale factor in which matter and radiation density are equals.

In matter era $\omega = 0$ so equation (2.44) become:

$$\Phi'' + \frac{6}{\eta}\phi' = 0 \quad (2.49)$$

We notice from the equation above that in matter dominated Universe, the gravitational potential is scale independent.

Before the CMB the ordinary matter or the baryons were tightly coupled with photons. However, the dark matter does not behave in the same way. In fact, it doesn't interact with light particle but only respond to gravity. So they have already been able to cluster under gravity before the decoupling epoch. The evolution of the density perturbation of dark matter in the early period of the Universe is governed by:

$$\frac{d^2\delta_m}{dy^2} + \frac{2+3y}{2y(1+y)} \frac{d\delta_m}{dy} - \frac{3}{2y(1+y)}\delta_m = 0 \quad (2.50)$$

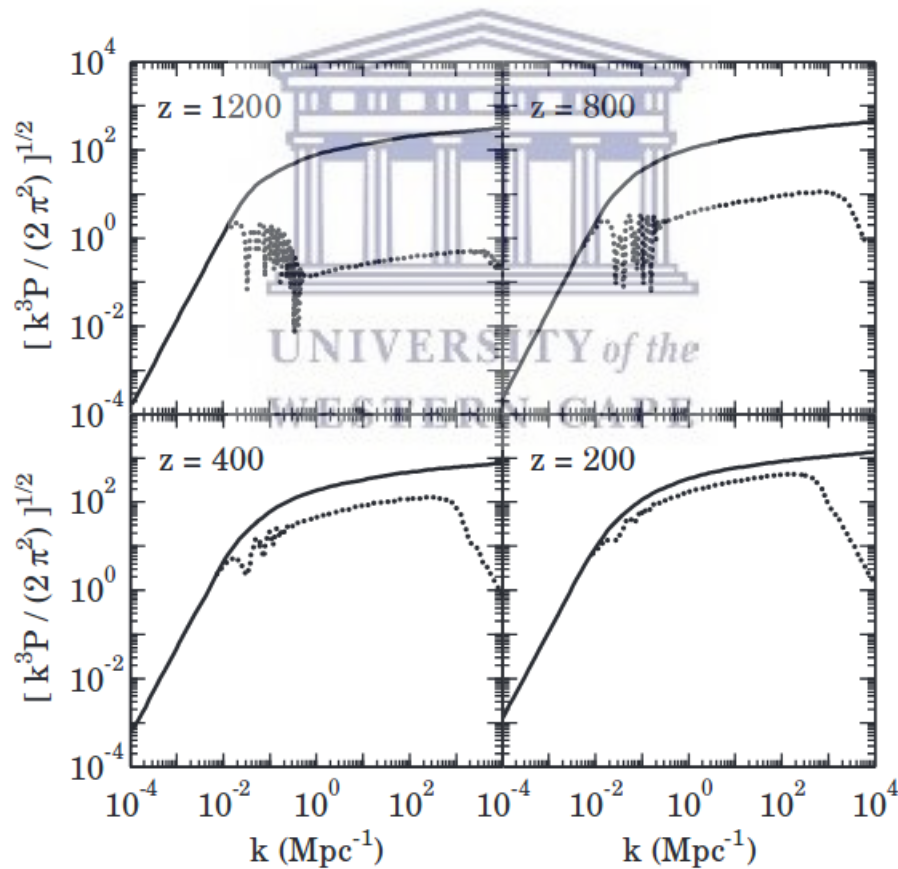


Figure 2.13: Evolution of the power spectrum before and after decoupling era. The dashed line represent the baryon and the solid line the dark matter. Image from [14]

After the decoupling era, the baryons start to cluster under gravity and so follow the evolution of dark matter to form the structures that we all know and observe today. We can see a clear view of the evolution of matter since the early time in figure 2.13. We can see in the figure that there is oscillation, in a specific scale, that we call the baryon acoustic oscillation. In fact it was produced due to the high pressure in the mixture baryon-photon before the recombination era. However as we can see, the baryons start to follow the dark matter as the Universe expand after the recombination epoch around $z = 1100$. Then the structure in the Universe continue to grow more and more and become those that we can see in our current era. The largest structure that we have observed is the so called "Saraswati supercluster" which is measured at redshift $z \sim 0.3$ [15] about 200 Mpc across. The Universe was initially homogeneous and isotropic with a small fluctuation which will grow over time under the unstable gravity forces in order to form the large scale structure that we observe today by the different survey such as the Sloan Digital Sky Survey (SDSS).

In the following sub-section we will summarize the different era during the history of the Universe.

2.1.3 Eras of evolution

- **Inflation**

Inflation era happened between the so called Grand Unified Theories (GUTs) era, which is a period where the three non-gravitational forces have not been separated yet, and the quark era. It is generally described as the almost exponential expansion of the Universe just after the Big Bang.

The comoving horizon is the maximum distance that light can travel from time $t = 0$ to a certain time t :

$$d_{\chi} = \int_0^t \frac{dt'}{a(t')} = \int_0^a \frac{da}{Ha^2} = \int_0^a d \ln a \left(\frac{1}{aH} \right) \quad (2.51)$$

The inflation model has the following key features:

- **Decreasing comoving horizon**

Inflationary model solved the horizon problem by stating that early on, the Universe had been in causal contact and so had the same property. In fact this means that there was a period when the comoving horizon, d_{chi} decreases and so the comoving Hubble radius $(aH)^{-1}$ as we can see in equation (2.51). This can be translated mathematically as:

$$\frac{d}{dt} \left(\frac{1}{aH} \right) < 0 \quad (2.52)$$

- **Accelerated expansion**

During the inflation, the Universe experience an accelerated expansion. In fact, this is actually a direct consequence from the shrinking of the co-moving horizon.

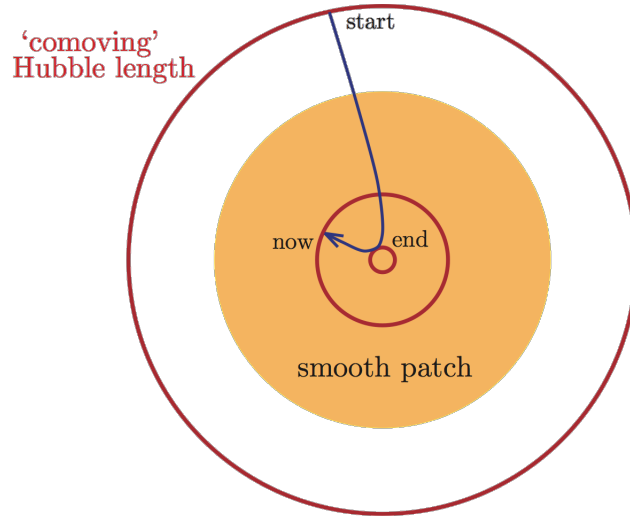


Figure 2.14: The shrinking of the comoving hubble radius during inflation and its expansion after. Credit [13]

$$\frac{d}{dt}(aH)^{-1} = -\frac{\ddot{a}}{(aH)^2}$$

(2.53)

UNIVERSITY of the
WESTERN CAPE

which implies directly that:

$$\frac{d^2 a}{dt^2} > 0 \quad (2.54)$$

– Negative pressure

From the second Friedmann equation, we have:

$$\frac{\ddot{a}}{a} = -\frac{4\pi G}{3}(\rho + 3p) \quad (2.55)$$

Hence:

$$p < -\frac{\rho}{3} \quad (2.56)$$

• Nucleosynthesis

After the inflation epoch, the Universe cooled down enough ($\approx 0.05 MeV/k_B$) to allow the formation of the first nuclei made by a proton and neutron. There was also formation of heavier element which is helium. We can see an example of the reactions of formation of the helium in the early time:



where 1_0n is a neutron.

• Recombination/decoupling era

This epoch occurred when the temperature of the Universe cooled down enough that the photon and the baryon decouple and finally be able to go freely in form of cosmic radiation that we measure today the remnant of it. It is known as the 'cosmic microwave background radiation' or CMB. Then the nuclei and electron that before were not be able to combine can finally interact together to start forming a new and more elements. We will describe more about this period later.

• Dark Ages

This is the epoch where the baryonic matter is mainly hydrogen but there was not yet any star that has been formed. The Universe at this time is completely dark and also dominated by dark matter which has grow without interacting with anything except gravity.

• **Reionization**

Reionization is the era where the first stars and quasars were born due to gravitational collapse. The neutral intergalactic medium is ionized by radiation from the stars and quasars.

For our study, we used Λ CDM model where the matter is composed by baryon and cold dark matter. We can see a clear illustration of the evolution and epoch of the Universe in figure 2.15 from the big bang to our present era.

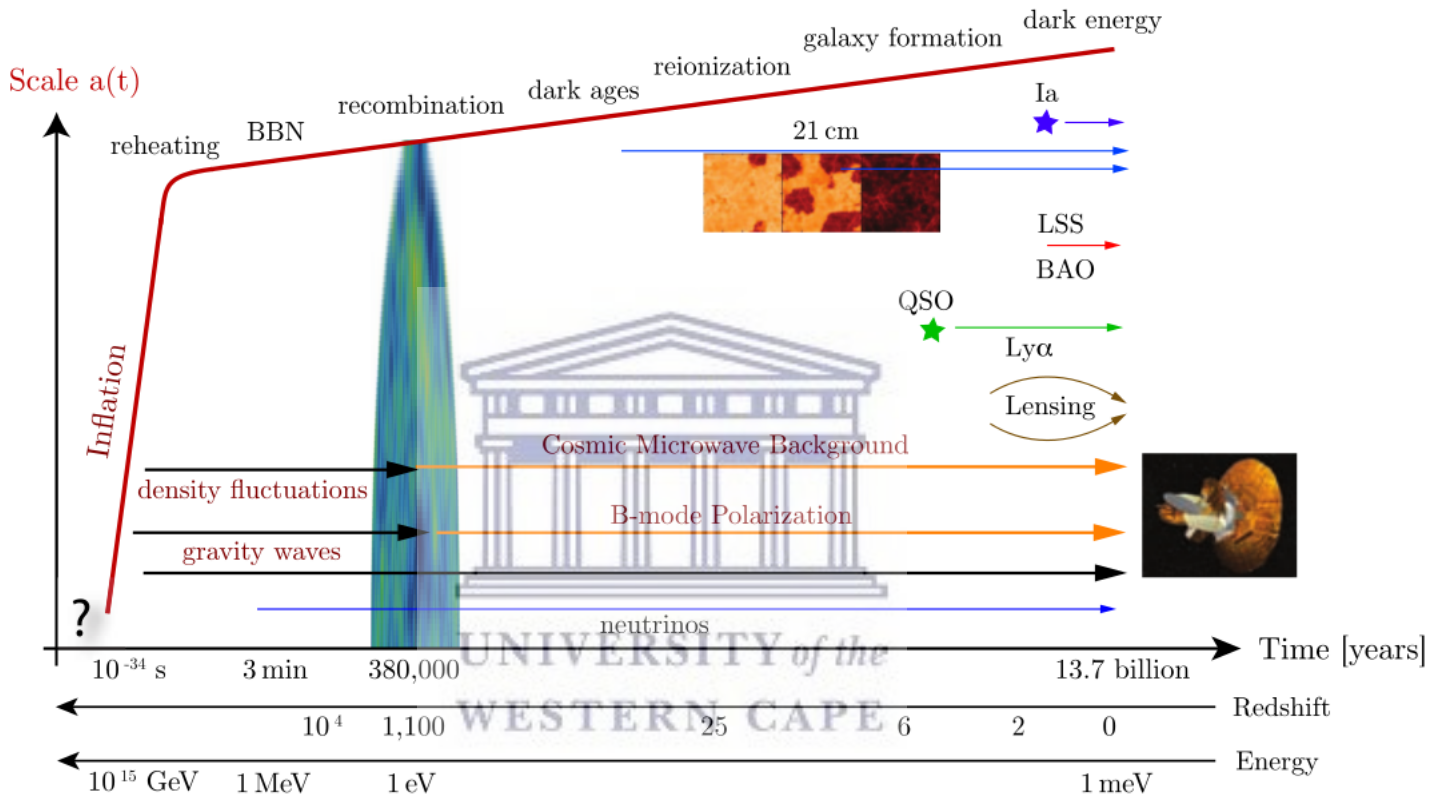


Figure 2.15: Evolution of the Universe through time and the major era that our Universe went through from the big bang to our present time. Diagram from [16]

2.2 Cosmological distance

In astronomy, we often define an object or an event from its redshift z in which we conclude that higher the redshift, the more far away is the object or event in question but also the earlier is it is. We can relate the redshift to distances depending on the type observation. in Cosmology, we often measure two type of distances: Angular diameter distance and luminosity distance. We can express those distances in term of the redshift z under certain conditions. In an observation, we need a reference object or property for a given measurement.

Firstly the standard candle are objects in which we know the absolute luminosity. We can then infer the distance by using the observed flux :

$$F_{obs} = \frac{L}{4\pi d_L(z)^2} \quad (2.61)$$

where d_L represent the luminosity distance. We often use cepheid variable and supernovae type Ia as standard candle. For standard ruler, we know the physical size so that we can compute the angular diameter distance by measuring an solid angle $\Delta\Omega$ subtented by the object. An example of standard ruler is the size of particle horizon during the recombination era. We compute it by using the following formula:

$$d_a^2(z) = \frac{\pi r^2}{\Delta\Omega^2} \quad (2.62)$$

where r is the physical radius.

They are related to the comoving distance d_c as follow:

$$d_a(z) = \frac{d_c}{z + 1} \quad (2.63)$$

$$d_L(z) = (1 + z)d_c \quad (2.64)$$

where the comoving distance d_c is defined as:

$$d_c = \int_0^z \frac{dz'}{H(z')} \quad (2.65)$$

where the $H(z)$ is the Hubble function that we describe in equation (2.29) assuming a flat Universe.

We can see the evolution of the distances with respect to the redshift z in figure 2.16. We notice that those two distances are the same locally (i.e. $z \ll 1$), since $d_L = (1 + z)^2 d_a$ ¹, however for high-redshift it is not the case. We use those distances for different purposes , in fact in order to get the luminosity of given celestial object, we have to use the luminosity distance since they are related as we can see in equation (2.61). The same things goes for the angular diameter distance, if we want to know the physical size of a source, we choose the angular diameter distance d_a according to its definition in (2.62).

¹The distance duality relation is valid for whatever cosmological model. It is even independant from the Einstein Field's Equation. It only depends on the following assumption:

- The curvature tensor should be Riemannian
- Number of photon should be conserved

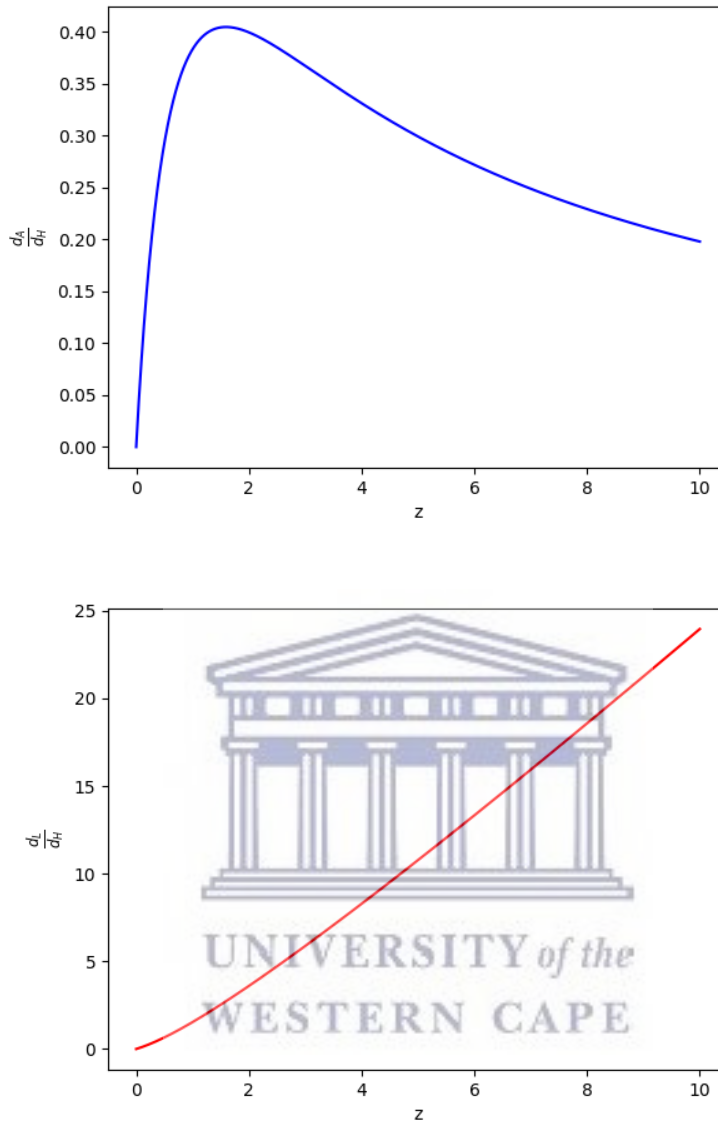


Figure 2.16: Evolution of the angular diameter (top) and luminosity distance (bottom) with respect to the Hubble distance d_H against redshift z .

2.3 2-point correlation function and power spectrum

The clustering of matter is described by the two point correlation function $\zeta(r)$. Its Fourier transform is the matter power spectrum $P(k)$. Its spherical harmonic transform is the angular power spectrum C_{ll} .

The 2-point correlation function is defined as:

$$\zeta(r) = \langle \delta(\vec{x})\delta(\vec{x} + \vec{r}) \rangle \quad (2.66)$$

The Fourier transform of the matter density contrast is defined by:

$$\delta_k = \int d^3x \delta(\vec{x}) \exp(i\vec{k}\vec{x}) \quad (2.67)$$

$$(2.68)$$

$$\delta_x = \int d^3k \delta_k \exp(-i\vec{k}\vec{x}) \quad (2.69)$$

So we can write:

$$\begin{aligned} \langle \delta_k \delta_{k'} \rangle &= \int \int d^3x d^3x' \langle \delta(\vec{x}) \delta(\vec{x}') \rangle \exp(i(\vec{k} - \vec{k}')\vec{x}) \exp(-i\vec{k}'\vec{x}') \\ &= (2\pi)^3 \delta(\vec{k} - \vec{k}') P(k) \end{aligned} \quad (2.70)$$

where \vec{r} is the distance between two points and so $P(k)$ is given by:

$$P(k) = \int d^3r \zeta(r) \exp(-i\vec{k}\vec{r}) \quad (2.71)$$

The matter power spectrum $P(k)$ is shown in figure 2.17.

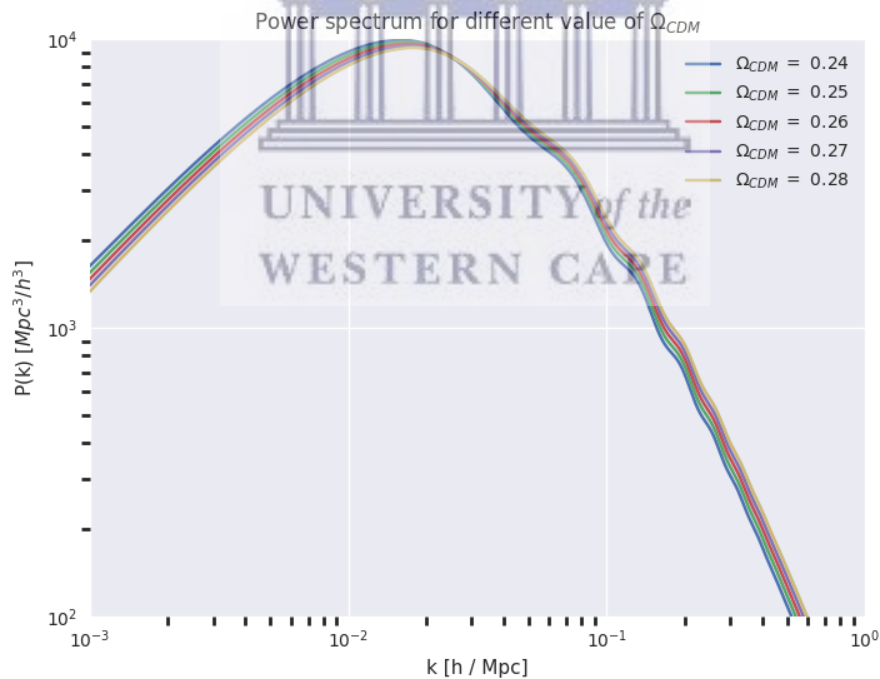


Figure 2.17: Plot of the matter power spectrum for different Λ CDM models

Relation between $P(k)$ and C_l :

If we project the field $\delta(\vec{x}, z)$ onto a sphere, we will have:

$$\delta(\vec{x}, z) = \sum_{l=0}^{\infty} \sum_{m=-l}^{m=l} a_{lm}(r(z)) Y_{lm}(\hat{n}) \quad (2.72)$$

where $\vec{x} = r(z)\hat{n}$ and so we can write also a_{lm} as following:

$$a_{lm} = \int d\Omega_n \delta(\vec{x}, z) Y_{lm}^*(\hat{n}) \quad (2.73)$$

and also that:

$$\int d\Omega_n Y_{lm}(\hat{n}) Y_{l'm'}^*(\hat{n}) = \delta_{ll'} \delta_{mm'} \quad (2.74)$$

We define C_{ll} via the harmonic coefficients of the density contrast:

$$\langle a_{lm} a_{l'm'}^* \rangle = C_l \delta_{ll'} \delta_{mm'} \quad (2.75)$$

$$\langle a_{lm} \rangle = 0 \quad (2.76)$$

In term of the mode k , a_{lm} can be defined as:

$$a_{lm} = \frac{1}{(2\pi)^3} \int \int d\Omega_n d^3 k \delta_k Y_{lm}^*(\hat{n}) \exp(-ikr \cos \theta) \quad (2.77)$$

where $\vec{k}\vec{x} = k r \cos \theta$. We have the following identity:

$$\exp(-ikr \cos \theta) = \sum_{l=0}^{\infty} (2l+1) (-i)^l \mathcal{L}_l(\cos \theta) j_l(kr) \quad (2.78)$$

where \mathcal{L}_l are the Legendre polynomials that satisfy the following relation:

$$\int d\Omega_n \mathcal{L}_{l'}(\cos \theta) Y_{lm}^*(\hat{n}) = \frac{4\pi}{2l+1} Y_{lm}^*(\hat{k}) \delta_{ll'} \quad (2.79)$$

So we can write a_{lm} as:

$$a_{lm} = \frac{(-i)^l}{2\pi^2} \int d^3 k \delta_k j_l(kr) Y_{lm}^*(\hat{k}) \quad (2.80)$$

where j_l is the spherical bessel function and by taking the conjugate of 2.80, we have:

$$\langle a_{lm} a_{l'm'}^* \rangle = \frac{(-i)^l i^{l'}}{4\pi^4} \int d^3 k \int d^3 k' j_l(kr) Y_{lm}^*(\hat{k}) Y_{l'm'}(\hat{k}') \langle \delta(\vec{k} \delta^*(\vec{k}')) \rangle$$

$$\langle a_{lm} a_{l'm'}^* \rangle = \frac{2}{\pi} \int k^2 dk j_l(kr) P(k) \delta_{ll'} \delta_{mm'} \quad (2.81)$$

$$(2.82)$$

So using the definition in 2.75, we have the expression for C_l which is:

$$C_l = 4\pi \int d\ln k j_l(kr) j_l(kr) \mathcal{P}(k) \quad (2.83)$$

where $\mathcal{P}(k)$ is the dimensionless power spectrum such that $\mathcal{P}(k) = k^3 \frac{P(k)}{2\pi^2}$.

If we take account the effect of the window function $W(z_1, z_2)$ in which we can see the plot in figure 2.18 for different windows, we have the following relation for a_{lm} :

$$a_{lm}^W(\bar{z}) = \frac{(-i)^l}{2\pi^2} \int d^3k dz W(\bar{z}, z) \delta_k j_l(kr) Y_{lm}^*(k) \quad (2.84)$$

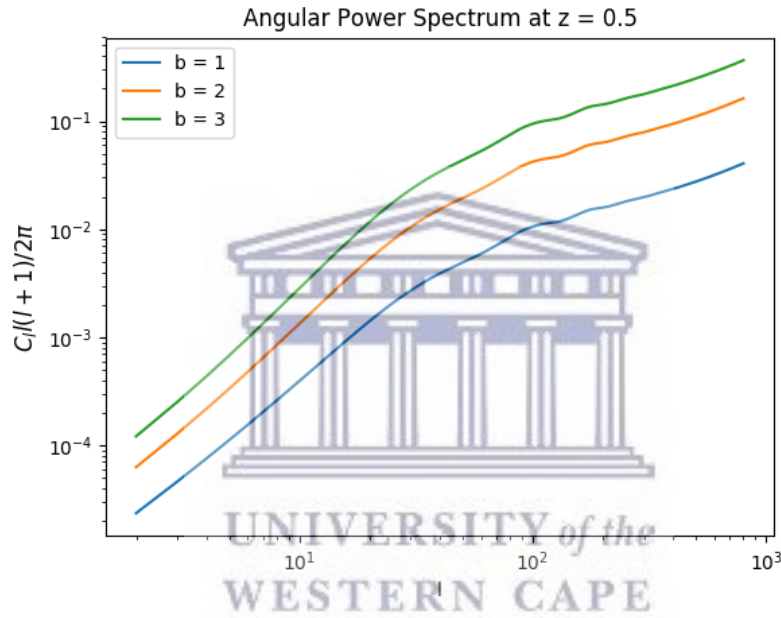


Figure 2.18: Angular power spectrum from CAMB at a centered redshift $z = 0.5$ for different value of the bias b .

2.4 The kinematic dipole

The isotropy of the Universe is an approximation for large scale. In fact we can see this anisotropy in $l = 1$ which is the first spherical harmonic. We move through the Universe as part of the Solar System, hence we shall see a slightly higher number of sources in the direction of our peculiar motion and they appear slightly brighter as well and a small deficit of sources in the opposite direction. In other words, the number count of radio sources are affected by two well known effects: Doppler effect and aberration effect. In this subsection, we will quantity how these effects modify the observed number counts, and thus produce a dipole anisotropy on them.

The number of observed sources per unit solid angle above a flux limit is defined by:

$$\frac{dN}{d\Omega}(> S) \propto S^{-x} \quad (2.85)$$

where $-x$ is a slope which is a free paramater that we fit later in figure 3.10 and S is the flux density such that:

$$S(\nu) \propto \nu^{-\alpha} \quad (2.86)$$

which α and ν are the spectral index and frequency. Due to the Doppler effect, we have:

$$\nu_{obs} = \delta \nu_{rest} \quad (2.87)$$

where:

$$\delta = \frac{1 + \frac{v}{c} \cos \theta}{\sqrt{1 - \left(\frac{v}{c}\right)^2}} \quad (2.88)$$

and the frequency with obs and rest subscript represent the observed and the rest frame frequency.

$$S_{obs}(\nu_{obs}) \propto \delta \nu_{rest}^{-\alpha} \quad (2.89)$$

Using the relation in 2.87, we have:

$$S_{obs}(\nu_{obs}) \propto S_{rest}(\nu_{obs}) \delta^{1+\alpha} \quad (2.90)$$

So we will have the final transformation:

$$\left(\frac{dN}{d\Omega}\right)_{obs} = \left(\frac{dN}{d\Omega}\right)_{rest} \delta^{x(1+\alpha)} \quad (2.91)$$

Now let see about the aberration effect. It's the change in position of the source due to our motion. So we have the following transformation for θ [17]:

$$\tan \theta' = \frac{\sin \theta \sqrt{1 - \frac{v^2}{c^2}}}{\frac{v}{c} + \cos \theta} \quad (2.92)$$

where θ' is the observed angle between the direction of motion and the target source.

For the solid angle we have:

$$d\Omega' = \sin \theta' d\theta' d\phi \quad (2.93)$$

where we have the following relation for $\sin \theta$ and $d\theta$:

$$\sin \theta' = \frac{\sin \theta}{\sqrt{1 + 2\frac{v}{c} \cos \theta}} \quad (2.94)$$

$$d\theta' = \frac{1 + \frac{v}{c} \cos \theta}{1 + 2\frac{v}{c} \cos \theta} d\theta \quad (2.95)$$

So using the equations 2.94 and 2.95 in 2.93, we will get:

$$d\Omega' = \frac{1 + \frac{v}{c} \cos \theta}{1 + 2\frac{v}{c} \cos \theta} \frac{\sin \theta}{\sqrt{1 + 2\frac{v}{c} \cos \theta}} \quad (2.96)$$

$$d\Omega' = d\Omega \left(1 - 2\frac{v}{c} \cos \theta\right) + O\left(\frac{v^2}{c^2}\right) \quad (2.97)$$

So if we combine this transformation to the Doppler effects in 2.91, we will have the final expression of the number count affected by both aberration and Doppler effects:

$$\left(\frac{dN}{d\Omega}\right)_{obs} = \left(\frac{dN}{d\Omega}\right)_{rest} \left(1 + [2 + x(1 + \alpha)]\frac{v}{c} \cos \theta\right) \quad (2.98)$$

The dipole amplitude is given by:

$$A = [2 + x(1 + \alpha)]\frac{v}{c} \quad (2.99)$$

In order to evaluate the radio dipole, we divide the map into two hemispheres where the symmetry axes are given by the pixels centres of the maps (3072 pixels here) and use the following estimators:

$$D = \frac{\sigma_u - \sigma_d}{\sigma_t} \quad (2.100)$$

where

$$\sigma_i = \frac{N_i}{2\pi f_i} \quad (2.101)$$

in which f_i is the sky fraction and N_i is the number of sources in hemisphere i ($i \in [u,d]$, u = north hemisphere and d = south hemisphere). We can see an illustration of the hemispheres in a given direction in figure 2.19.

$$\sigma_t = \frac{N}{4\pi f_t} \quad (2.102)$$

is the total density where N is the total number and f_t is the total fraction sky.

We do this for all direction in sky and then find the maximum of D and repeat the process for all the simulated maps. We can see the distribution of the dipole amplitude from the mocks in figure 2.20.

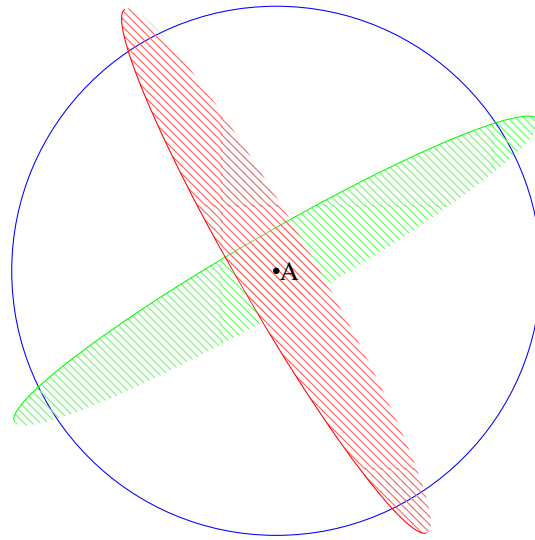


Figure 2.19: Sky sphere divided on two hemispheres by a plane in a given direction in the sky.

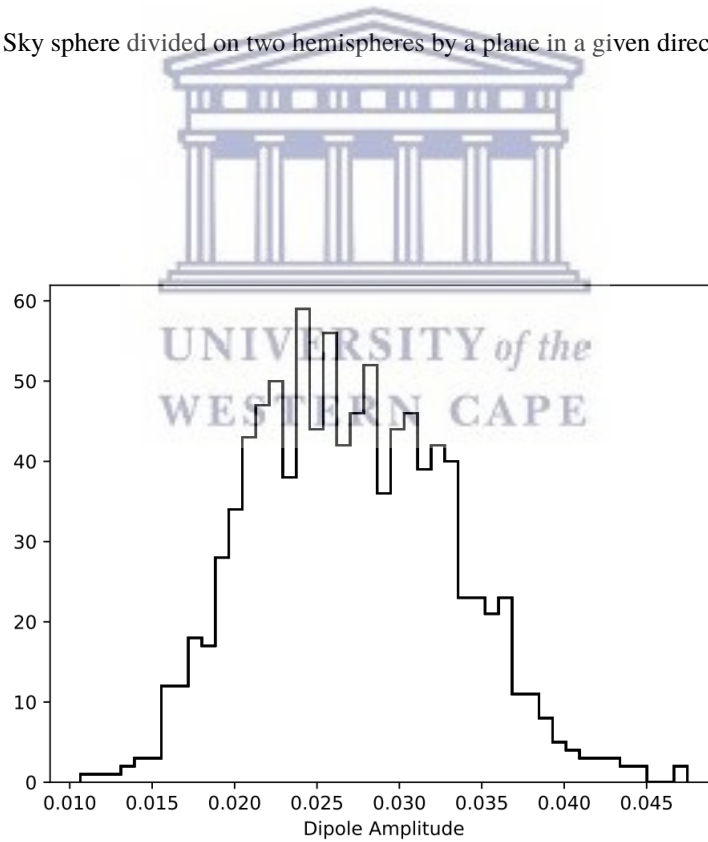


Figure 2.20: Distribution of the dipole amplitude of the mocks that have the same fiducial dipole as the data.

Analysis procedures

1 Visualisation and simulation tools

In this section, we discuss the main package and a simulation code that we used in this work which are: the Hierarchical Equal Area and iso-Latitude Pixelation or HEALPix (<http://healpix.sourceforge.net>) and the Full Lognormal Astro-fields Simulation Kits or FLASK code. We will talk first about the Healpix since FLASK depend on it also.

1.1 HEALPix

HEALpix is basically a representation of function on a sphere with high resolution. It is a very useful package for its easy visualisation and analysis of data in a sky map considered as sphere. However the discretisation of full sky must satisfies the following mathematical requirements where we can see the detail about each of them in [18]:

- Hierarchical structure of the data base
- Equal areas of discrete elements of partition
- Iso-Latitude distribution of discrete area elements on a sphere

In fact, HEALPix is defined by 3 parameters that are related to each other:

- N_{side} : paramater that define the resolution of the grid and so define the number of divisions of the resolution pixel:

$$N_{side} = 2^k \quad (3.1)$$

where $k \in \mathbb{N}$

- N_{pix} : Number of pixel in the grid in which the resolution has been define by N_{side} , given by:

$$N_{pix} = 12 N_{side}^2 \quad (3.2)$$

So the pixel number p is such that $p \in [0, 12N_{side}^2]$.

- N_{ring} : Number of the ring in which the center pixels have the same latitude in the map. It can be expressed as :

$$N_{ring} = 4N_{side} - 1 \quad (3.3)$$

We can see in figure 3.1, the representation of the base-resolution, which has 12 pixels, on plane in which x_s and y_s runs along longitude and latitude [19]. Notice also that the pixels area are given by:

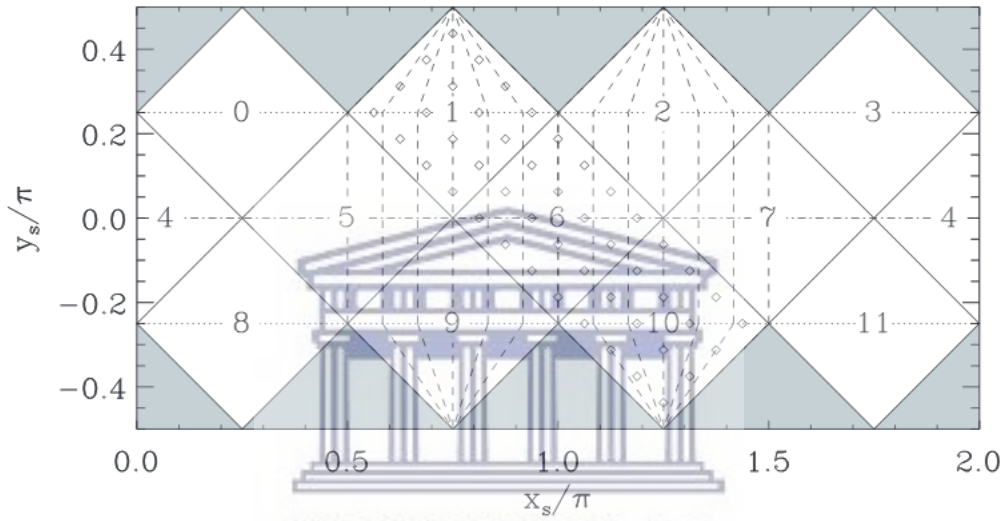


Figure 3.1: Projection on the plane of the base resolution HEALPix pixels $N_{side} = 1$. Image from [19]

$$\begin{aligned} \Omega_{pix} &= \frac{4\pi}{N_{pix}} \\ &= \frac{\pi}{3N_{side}^2} \end{aligned} \quad (3.4)$$

For the coordinate, HEALPix has its own definition which is slightly different compare to the International Astronomical Union or IAU. In fact we can see in figure 3.2 in which we can see the way how the spherical coordinate is represented in both system.

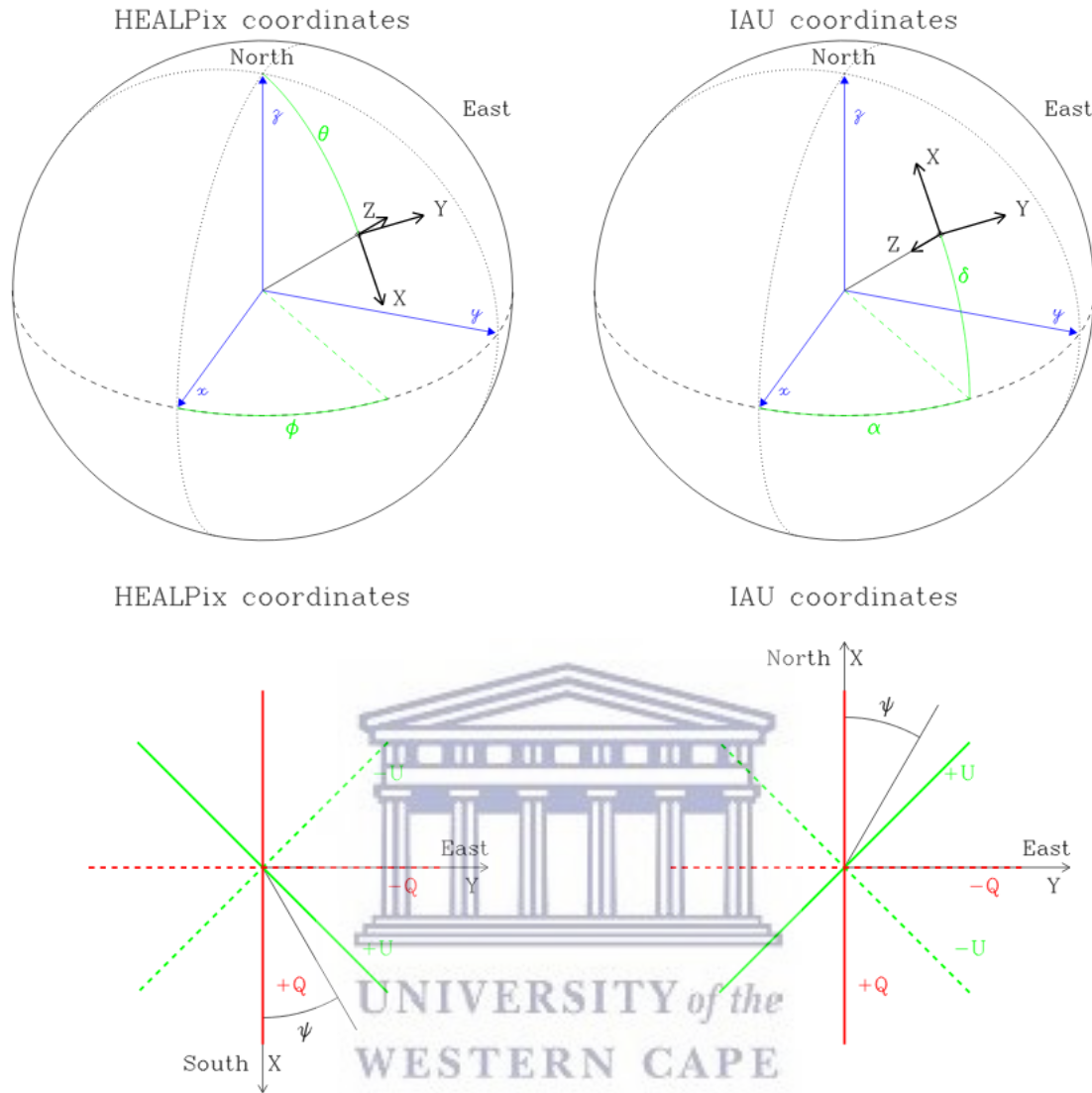


Figure 3.2: Spherical coordinate measurement in HEALPix and IAU coordinate system. Credit: <https://healpix.jpl.nasa.gov/html/intronode12.htm>

The HEALPix software package has routines that are written in different languages such as: C, C++, Fortran, IDL, Python and Java. Here we are going to use the Python version known as Healpy (<http://pypi.python.org/pypi/healpy>).

1.2 FLASK

The Full Lognormal Astro-fields Simulation Kits or FLASK is a simulation code that has a routine written in C++ language. We can see the full details of this software in [20]. It is a very useful software since it can produce a full lognormal simulated sky map of astrophysical fields such as matter, arbitrary tracer densities (galaxies, quasars, dark matter haloes) in which the observer is located at the center. FLASK slices the Universe which is represented as a three-dimensional space into spherical shells around the observer. In fact, the slices are discretized by the HEALPix package that we describe in the previous section. In figure 3.3,

we can see the algorithm that illustrate how FLASK work in the background. As we can see in the chart, it takes as input angular power spectrum but also a defined redshift distribution in which we can see the details of the procedure in the next section.

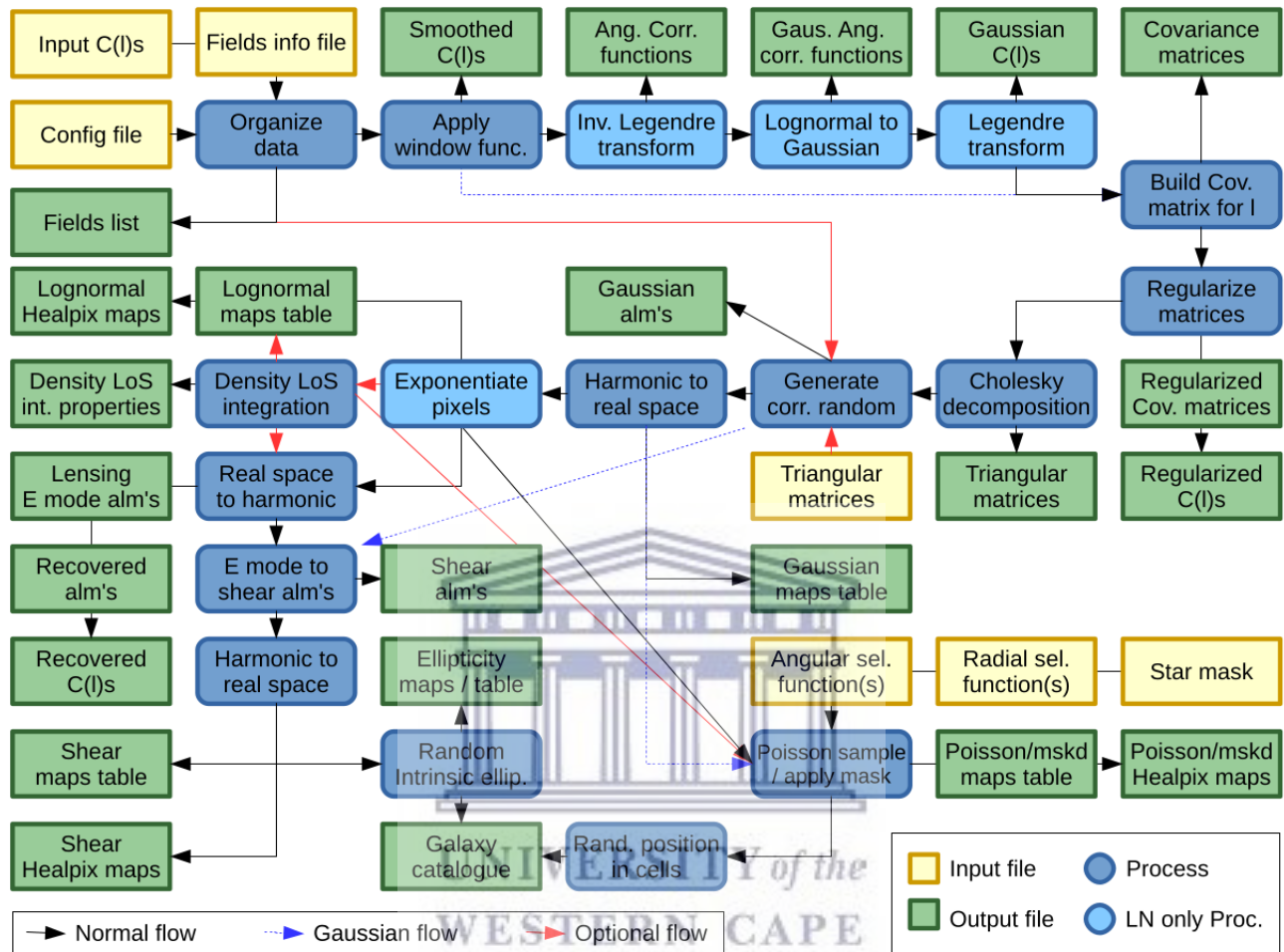


Figure 3.3: FLASK basic flow chart. Credit: [21]

2 Procedure analysis technique

2.1 The NVSS survey

The data that we will use come from the radio continuum survey NRAO VLA Sky Survey known as NVSS at 1.4 GHz [22] that we can see in Figure 3.4. For this analysis, we choose a flux cut

$$20\text{mJy} < S < 1000\text{mJy} \quad (3.5)$$

in which we mask the galactic plane and the region where we do not have data.

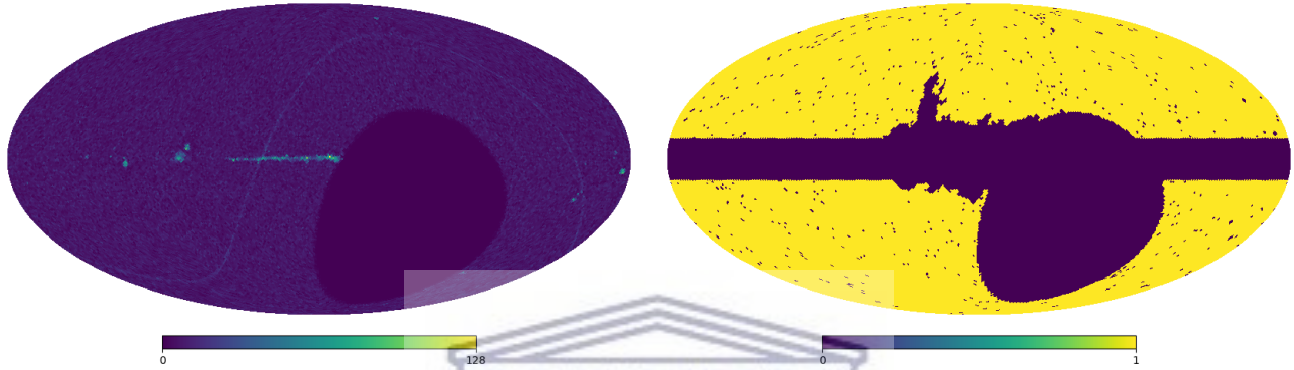


Figure 3.4: Pixelised number counts map from NVSS catalog and the mask that has been applied.

Then we produce simulated data that matches the NVSS number count using FLASK [23]. We compute the angular power spectrum from CAMB Sources ([24]) assuming a Λ CDM model.

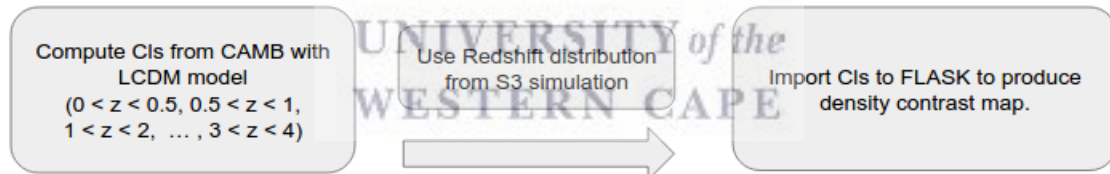


Figure 3.5: Steps of the simulation procedure.

For the galaxy redshift distribution in figure (3.7), we got it from S^3 (SKA Simulated Skies) ([25]) which follows the model:

$$\frac{dN}{dz} = \left(\frac{z}{a_1}\right)^{a_2} e^{-\left(\frac{z}{a_3}\right)^{a_4}} \quad (3.6)$$

Indeed it is almost in perfect agreement with the fitting function used in [26] in the equation (3.7):

$$\frac{dN}{dz} = n_0 \left(\frac{z}{z_0}\right)^\beta e^{-\beta \frac{z}{z_0}} \quad (3.7)$$

where fitted parameters are:

$$\begin{aligned}
 a_1 &= 30.89483209, \\
 a_2 &= 1.30544264, \\
 a_3 &= 0.37036427, \\
 a_4 &= 0.75130503, \\
 n_0 &= 0.00358338, z_0 = 0.80742509 \text{ and } \beta = 0.93674574
 \end{aligned}
 \tag{3.9}$$

The galaxy density contrast is given by:

$$\delta_{gi} = \frac{n_i}{\bar{n}} - 1
 \tag{3.10}$$

where \bar{n} is the average number count per redshift bin that can be obtained using equation (3.6) and n_i is the number count in pixel i . Two examples of the number count density contrast maps in the redshift ranges of $0.5 < z < 1.0$ and $2.0 < z < 3.0$ are exhibited in Figure 3.6, while in Figure 3.7, we show the pixelised density contrast maps for $0.0 < z < 4.0$



Figure 3.6: Mock map by FLASK for $0.5 < z < 1$ (left) and $2 < z < 3$ (right)

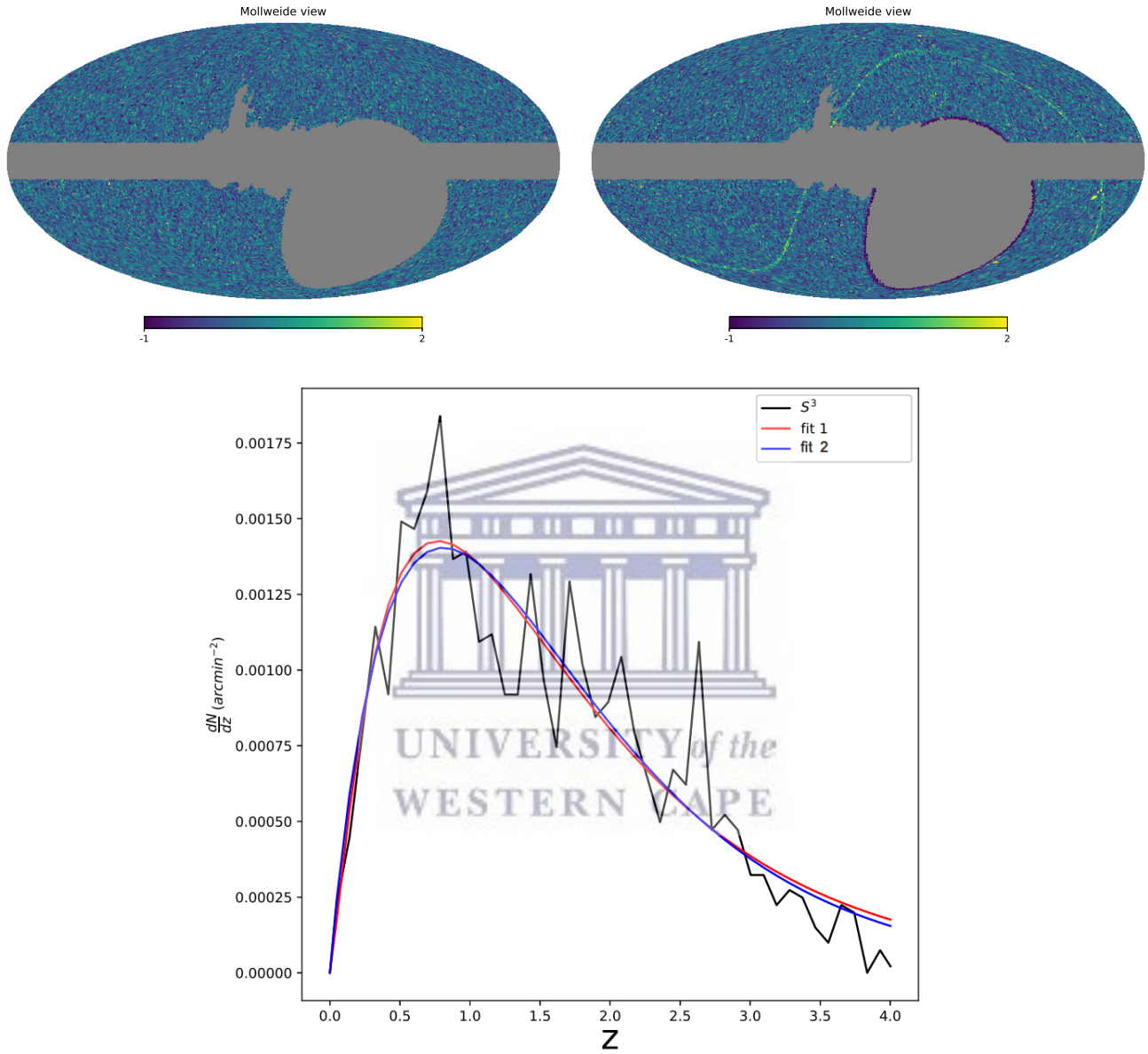


Figure 3.7: Top: Density contrast map for $0 < z < 4$ with $N_{\text{side}} = 64$ of one of the mock (left) and the data (right). Bottom: Simulated number count per redshift bin per square arcmin in black and its best fit based on the parametric equation (3.6) in red and the parametrized redshift distribution used in the planck results [26] in blue.

Then we compare the real NVSS data with the mock maps that mimick the expected $n(z)$ and $b(z)$ that we can see the evolution in the figure 3.8.

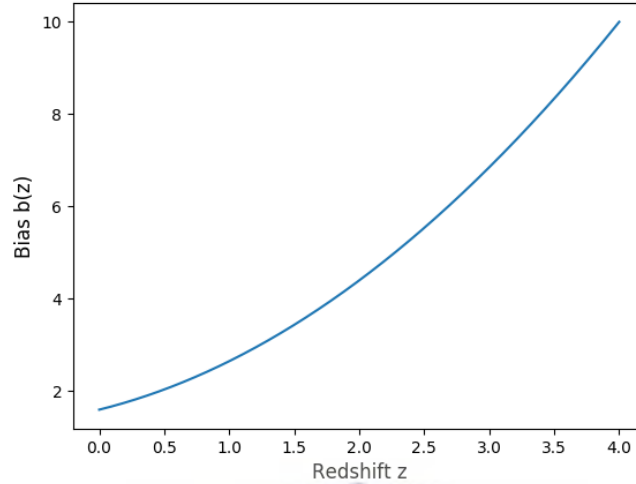


Figure 3.8: Evolution of the redshift bias

We can see the averaged angular power spectrum of the mocks with the poisson noise and the data in figure 3.9 in which the uncertainty is given by:

$$\sigma_{C_l}^2 = \frac{2C_l}{f_{sky}(2l + 1)} \tag{3.11}$$

where f_{sky} is the sky fraction and l the multipole.

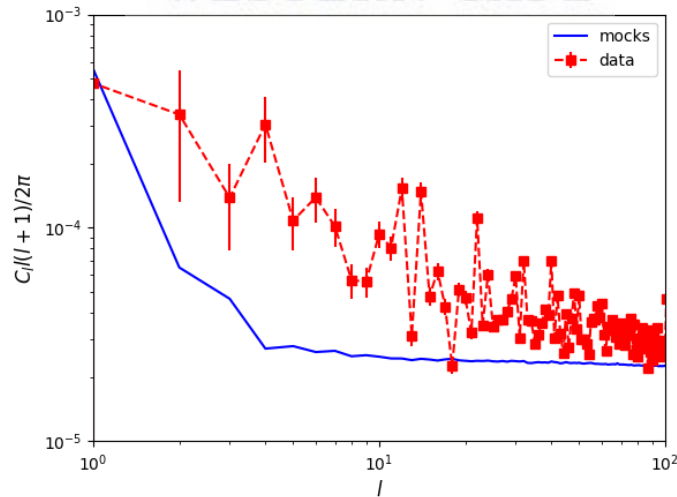


Figure 3.9: Angular power spectrum of the data in red and the mock data after the large scale structures, as well as shot noise, are included in the mock data number counts.

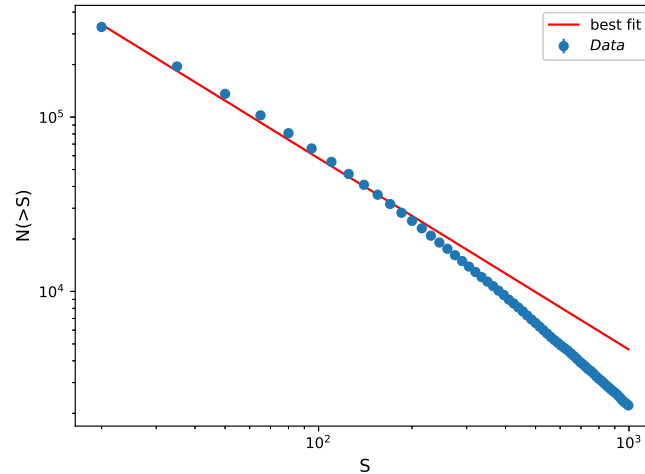


Figure 3.10: Total number of galaxies with respect to the a defined flux cut.

We can see in the figure 3.10 the distribution of the number count with respect to a given flux cut 2.85 from $S = 20$ mJy in which we can estimate the error as $\sigma = \sqrt{N(> S)}$. We can see that as we go further for the flux cut, we notice that we have decreased number of sources. Indeed after the fitting of $N(S)$, we have $x = 1.098$.

2.2 Testing the isotropy of the NVSS map

In this section we focus on testing the anisotropy of the Universe using number count maps. In order to do that, we need to define some statistical estimators. Here we are going to use the Analysis Of Variance test. To test the isotropy of the Universe, we adopt some of the idea in [3]. We choose smaller resolution ($N_{side} = 16$) for sake of computational reasons. Indeed we take randomly 3072 patches on the sky for a given radius r (here $r = 15^\circ, 20^\circ, 25^\circ, 30^\circ$) and we will save the location of those patches. Then for each patch, we choose a different rejection criteria RC (here we have $RC = 10\%, 30\%, 50\%$) in which we reject ($> RC$) or tolerate ($< RC$) a masked patch.

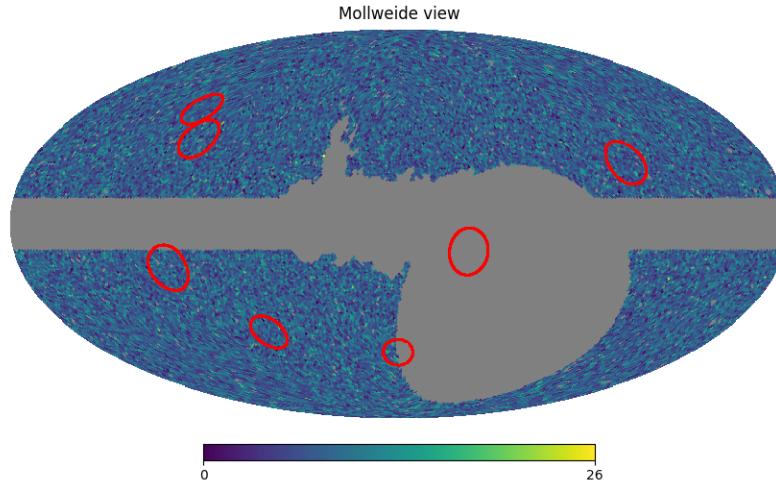


Figure 3.11: Number count map with some of the 1000 patches randomly distributed.

Then for each patch, we extract some statistical features such as mean and variance where we have:

$$\sigma_i^2 = \frac{1}{N_i - 1} \sum_{j=1}^N (k_{ji}^2) - M_i^2 \quad (3.12)$$

where k_{ji} is the number count in a pixel j in patch i , N_i and M_i are the number of pixels and the average number count per pixel in a patch i respectively.

In order to see variability between the data and the mocks, we produce a plot of the coefficient of variation cv , which is the scaled measure of the spread, in figure 3.12.

We compare the result between each patches using the ANOVA (Analyse of Variance) method which consist of a comparison of the mean number between and within the patch.

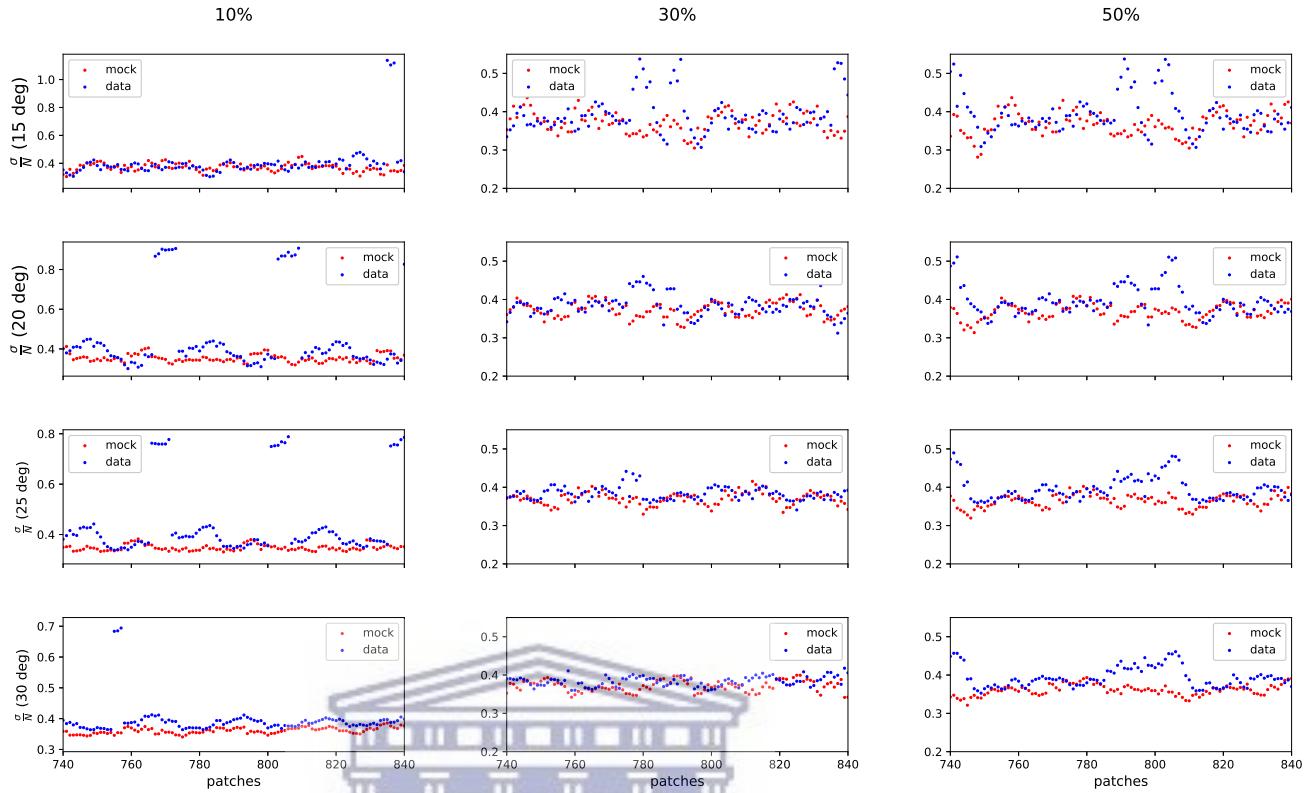


Figure 3.12: Coefficient of variations for each patches of the mocks and data for 100 patches for easy visualization.

2.3 ANOVA-test

ANOVA is a collection of methods for comparing multiple means across different treatments or groups [27]. Like most of statistical test, it consist of making a decision in which we accept or reject the null hypothesis, also depending on the degree. In order to do the test, we will need the F-test which is one of the most known statistic estimator. We can see in table 3.1, the basic idea of the test but we can summarize the way to compute it as following (<http://www.statisticshowto.com>):

The final goal for the ANOVA is an F-ratio	$F = \frac{\text{Variance between patches}}{\text{Variance within patches}}$
Each variance in the F-ratio is computed as SS/df	$V_b = \frac{SS_{\text{between}}}{df_{\text{between}}} \quad V_w = \frac{SS_{\text{within}}}{df_{\text{within}}}$

Table 3.1: The structure and sequence of calculation for the ANOVA from [27].

- Find the mean number count for each groups M_i .

$$M_i = \frac{\sum_{j=1}^N k_{ji}}{N_i} \tag{3.13}$$

where k_{ji} is a measurement of sample j and N_i is the number of sample in a group i .

- Find the overall mean OM (the mean of the groups combined).

$$OM = \frac{\sum_{i=1}^n M_i}{n} \quad (3.14)$$

where n is the number of groups.

- Find the Within Group Variation V_w

$$V_w = \frac{SSW}{dfw} \quad (3.15)$$

$$SSW = \sum_{i=1}^n \sum_{j=1}^N (k_{ji} - M_i)^2 \quad (3.16)$$

where dfw (the degree of freedom within the group) is: $dfw = n(N - 1)$ and k_{ji} is a measurement of a sample j in group i .

- Find the Between Group Variation V_b

$$V_b = \frac{SSB}{dfb} \quad (3.17)$$

$$SSB = \sum_{i=1}^n N(M_i - OM)^2 \quad (3.18)$$

where dfb (the degree of freedom between the group) is $dfb = n - 1$. V_b is the deviation of each Group Mean from the overall mean.

- Find the F statistic: the ratio of Between Group Variation to Within Group Variation.

$$F = \frac{V_b}{V_w} \quad (3.19)$$

In our case, the null hypothesis is the isotropic Universe. The groups represent the patches on the sky map and the k_{ji} is the number count per pixel j in a patch i .

Results and discussions

1 F-statistic

As we can see in equation (3.19), F-ratio is always positive since the numerator and denominator are both variances alike and so if the null hypothesis is true, the ratio should be near 1. So obviously the distribution of the F-ratio should peak around 1 depending on the degree of freedom. Indeed, our F-distribution in which the null hypothesis is true is given by the distribution of the F-ratio of the mock maps (theoretically isotropic). In order to make a statistical decision out of a test, we have to define a critical value of the F-ratio or F_{critic} . In fact, F_{critic} is a cut-off value in which we accept or reject the null hypothesis and depend also on the degree freedom of the numerator and the denominator given a value of α (confidence level) which can be chosen arbitrary. However, we can not really compare the F-statistic to exactly 1 but instead we will use the F-distribution of the mocks which assume a statistically isotropic Universe.

In figure 4.1, we can see that all the F-distribution of the mocks, as represented by the black line peak at around 1. We notice also from that figure that the F distribution of the mocks present a larger tail-end as we increase the radius size. In fact this is expected since the shape of the distribution depends on the degree of freedom, however we have smaller number of accepted patches. This implies a smaller number of the degrees of freedom between group or patches, which hence affects the distribution of the F-value and so its shape.

In the figure, we can see also that the F-statistic of the data (represented by the red lines) are far from the mean value of the mocks (green dashed line) except for the large patches. Indeed in figure 4.1, we can see that for small patches. This could be explained by the large number count that we can see in the pixelised number count map in figure 4.3. However after masking the region with high number count in figure 4.4, we have a value of the F-statistic of the data which become closer to the average value of the mock that is statistically isotropic. Indeed we expect to see this result since if we do an observation in a big angle of view, we will likely have a more isotropic phenomena than if we take a look with a small patch which present a bit of fluctuation in the number count distribution. However we can say that overall, there is no much evidence of a statistical anisotropy.

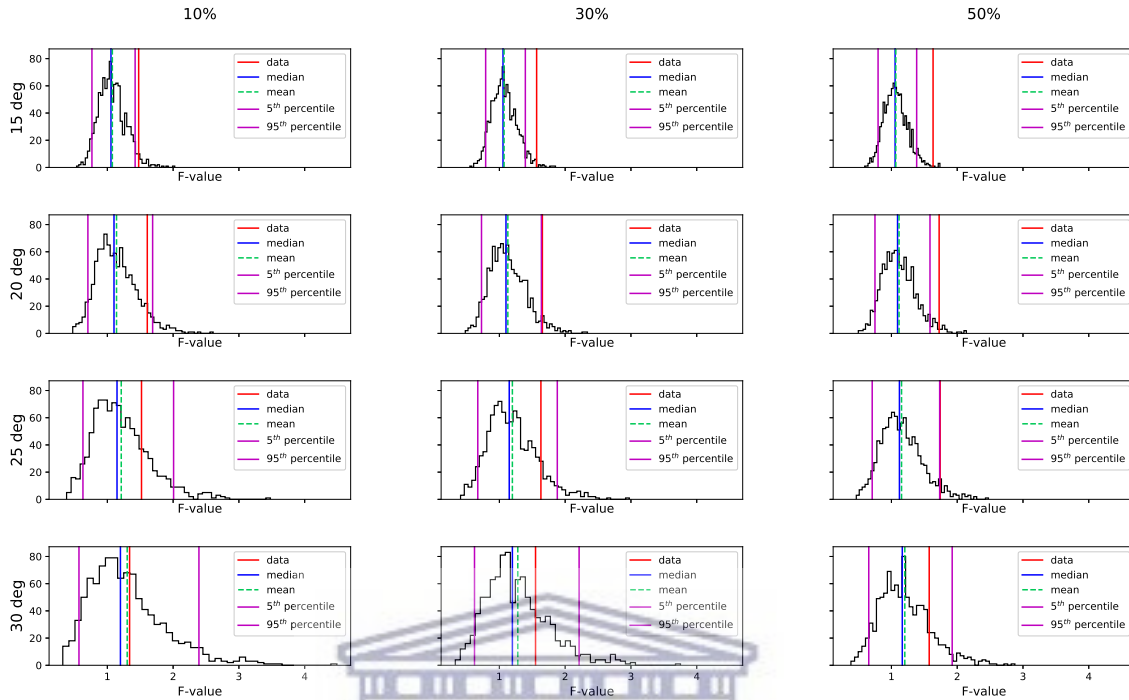
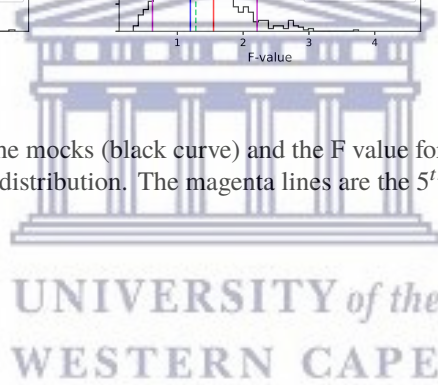


Figure 4.1: Distribution of the F-ratio of the mocks (black curve) and the F value for the data. We have also the mean (dashed green) and the median (blue curve) of the distribution. The magenta lines are the 5th and 95th percentiles since here we don't have a normal distribution



2 Local variance

The local variance is a more direct method to see the deviation of the mean across the sky with respect to the mocks. It can be defined as:

$$LV = \frac{(\frac{\sigma}{M})_{data} - (\frac{\bar{\sigma}}{M})_{mock}}{(\frac{\bar{\sigma}}{M})_{mock}} \quad (4.1)$$

where $\frac{\sigma}{M}$ is the coefficient of variation in which σ and M represent respectively the standard deviation of the number count per pixel per patch and the average number count per pixel per patch.

python

As we can see in figure 4.2, there is a large fluctuation in the direction $(\theta, \phi) = (207.125^\circ, -17.83940455^\circ)$. In fact around these region, the data does have a large number of sources than in other directions. We can clearly see it in the map in figure 4.3 in which the large number count is surrounded by blue curve.

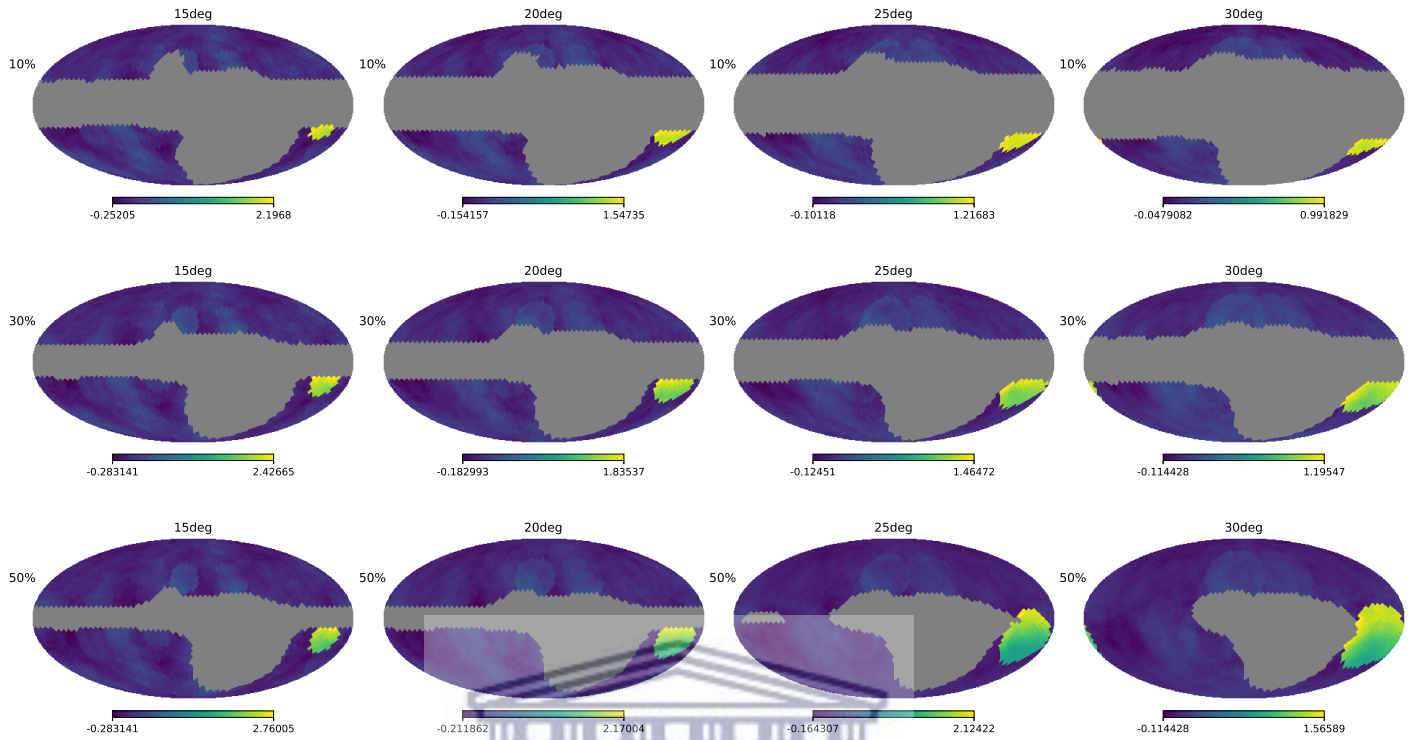


Figure 4.2: Local variance map given by the equation (4.1) for different radius and rejection criteria

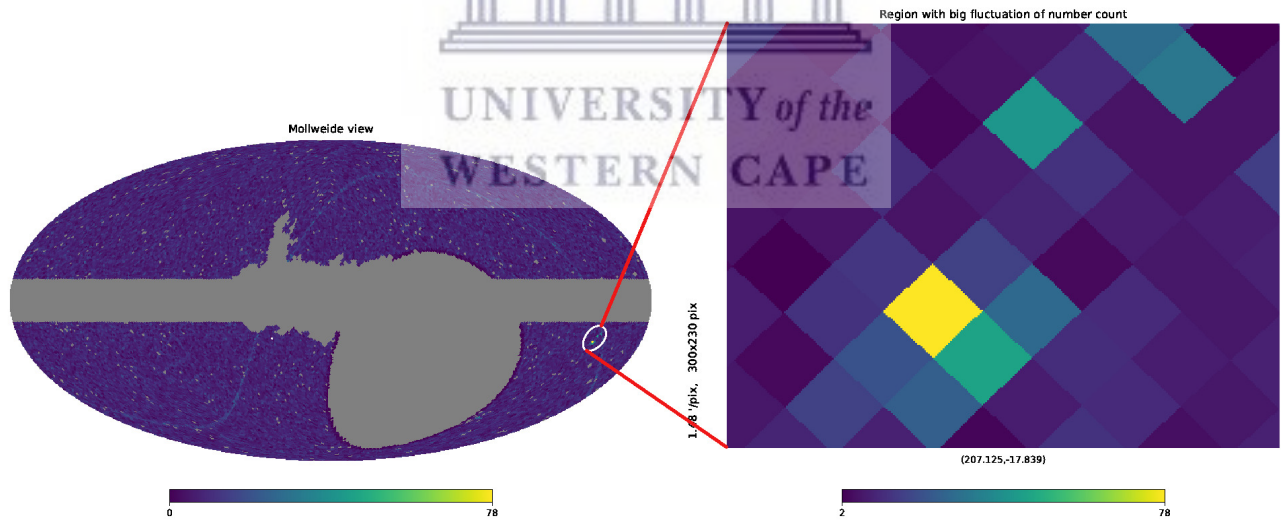


Figure 4.3: Number count map of the data with $N_{\text{side}} = 64$ in which we can see the large number count in the white circle.

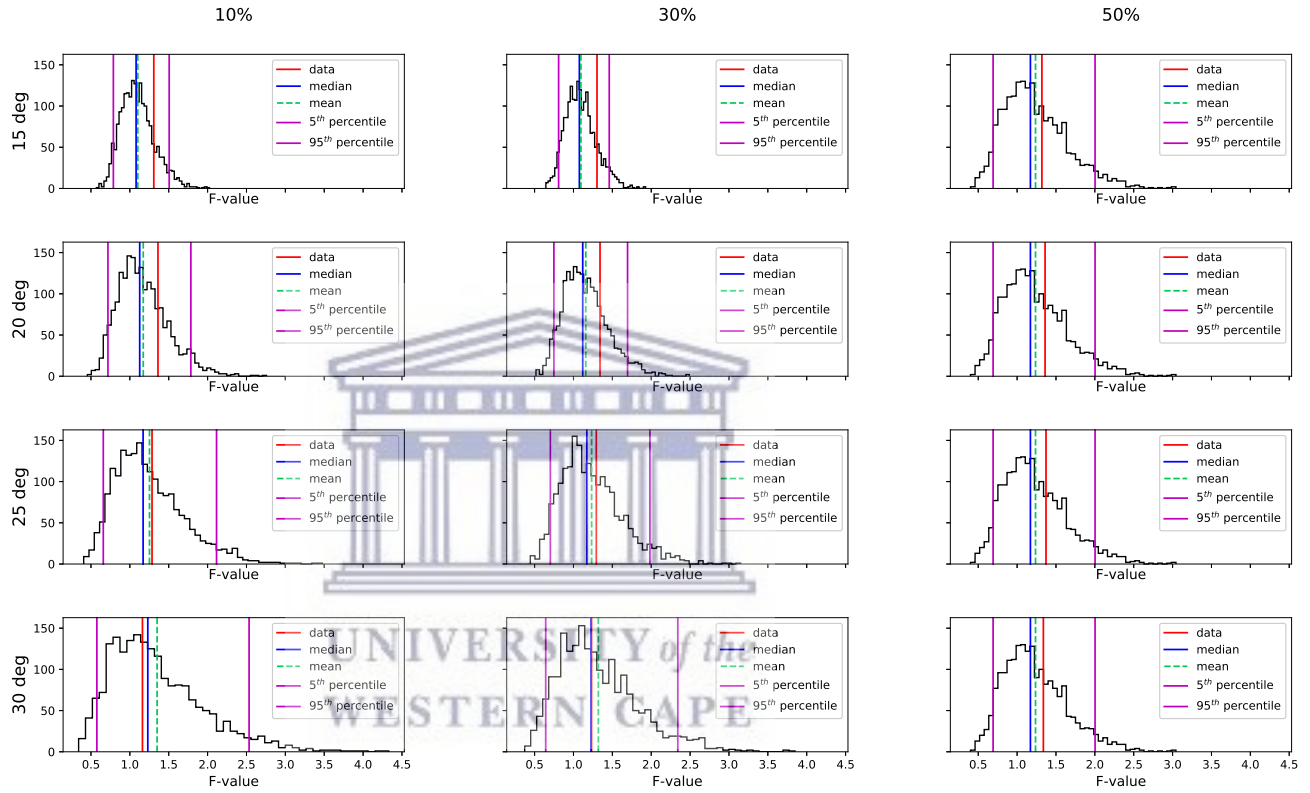


Figure 4.4: Distribution of the F-ratio of the mocks (black curve) and the F value for the data. We have also the mean (dashed green) and the median (blue curve) of the distribution. The magenta lines are the 5th and 95th percentiles since here we don't have a normal distribution

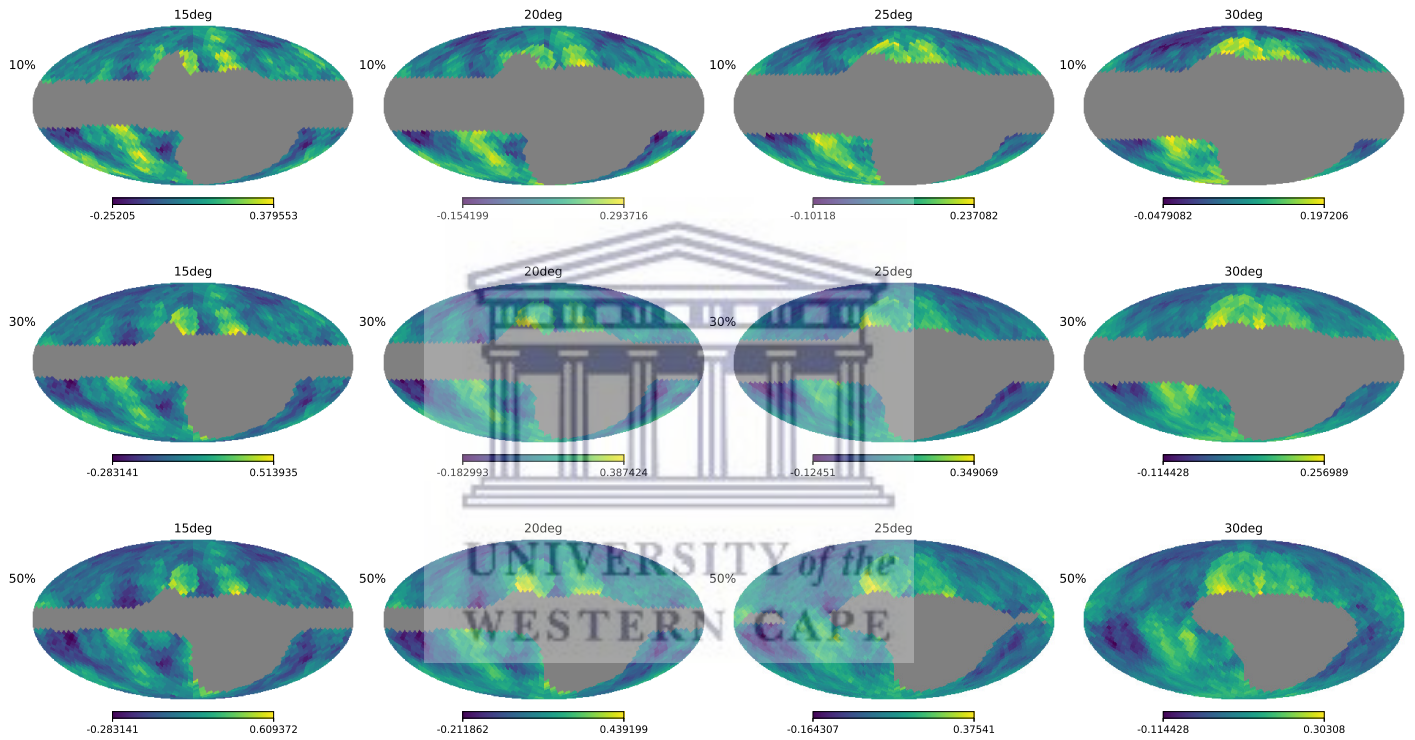


Figure 4.5: Local variance map of NVSS after masking the region with high variation of number count in the data.

Conclusion

In this project, we have analysed the isotropy of the Universe using a simulated sky map assuming a Λ CDM model. We used FLASK code to produce NVSS synthetic number count maps assuming a lognormal distribution, and based on the angular power spectrum from CAMB sources assuming the latest Planck's best fit in which we apply also a fiducial dipole seen in the real data. We did compare also the result with a real data from a radio survey like the NVSS. In order to do so, we draw patches across the sky with different radius size and rejection criterion, and apply a local variance estimator, in addition to the ANOVA test, to verify whether the real data is consistent with the mock data-sets as they are statistically isotropic by construction.

We found that the observed radio counts are consistent with the statistical isotropy hypothesis since the data agrees with the mock maps produced. We saw that the data was consistent with the mock maps that we produced. We obtained that, as we increase the patch radius, the discrepancy between the data and simulations become smaller, as we encompass a larger number of sources, thus the shot noise is reduced. In addition, we noticed that the more rigorous we were in terms of the rejection criterion of masked pixels, the better is the agreement between the real data and statistically isotropic realisations. Hence, we conclude that the optimum choice for patch radius and rejection criterion is 25° and 30%, respectively.

We have also estimated the dipole due to our motion after including the fiducial dipole from NVSS survey, using the same estimator as previous works, where the radio dipole are also similar to the analysis performed here is totally general and can be applied to any sort of cosmological observations. other analysis. Therefore, when larger and more complete data-sets become available, like EMU, SKA - or even optical surveys like LSST and Euclid - we should be able to greatly enhance the quality of this analysis, and carry out a precise test of statistical isotropy.

Appendices



UNIVERSITY *of the*
WESTERN CAPE

Useful Astronomical Units

Units	SI
Astronomical unit	$1.49597870 \times 10^{11} \text{ m}$
Parsec (pc)	$3.09 \times 10^{16} \text{ m}$
Megaparsec (Mpc)	$3.09 \times 10^{22} \text{ m}$
Light year (Ly)	$9.46 \times 10^{15} \text{ m}$
Solar mass (M_{\odot})	$1.989 \times 10^{30} \text{ kg}$
Jansky (Jy)	$10^{-26} \text{ W Hz}^{-1} \text{ m}^{-2}$

UNIVERSITY of the
WESTERN CAPE

B

CHAPTER

Astronomical and Cosmological constants

Constant	value
Speed of light c	2.9979245×10^{10} cm/s
CMB temperature T_0	2.725 K
Hubble constant H_0	$100h$ km s^{-1} Mpc^{-1}
Critical density ρ_c	$1.879h^2 \times 10^{-29}$ g cm^{-3}
Scale factor at equality a_{eq}	$4.15 \times 10^{-5} (\Omega_m h^2)^{-1}$
Wavenumber at equality k_{eq}	$0.073 \Omega_m h^2 Mpc^{-1}$
Boltzmann constant k_B	$8.617\ 3303 \times 10^{-5}$ eV/K
Newton's constant G	6.67428×10^{-8} $cm^3 g^{-1} s^{-2}$

Special functions

In this section, we are going to describe some of the special functions used in this thesis.

1 Legendre polynomials

The Legendre polynomial represented by $\mathcal{L}_l(\mu)$ is an l^{th} order polynomial of μ . It can be defined as follows:

$$(l + 1)\mathcal{L}_{l+1}(\mu) = (2l + 1)\mu\mathcal{L}_l(\mu) - l\mathcal{L}_{l-1}(\mu) \quad (\text{C.1})$$

where its values for the early l are:

$$\mathcal{L}_0(\mu) = 1, \mathcal{L}_1(\mu) = \mu, \mathcal{L}_2(\mu) = \frac{3\mu^2 - 1}{2} \quad (\text{C.2})$$

However the Legendre polynomial also has its specific properties which we can see below:

$$\mathcal{L}_l(-\mu) = (-1)^l \mathcal{L}_l(\mu) \quad (\text{C.3})$$

$$\int_{-1}^1 \mathcal{L}_l(\mu) d\mu = 0 \quad (\text{C.4})$$

$$\int_{-1}^1 d\mu \mathcal{L}_l(\mu) \mathcal{L}_{l'}(\mu) = \delta_{ll'} \frac{2}{2l + 1} \quad (\text{C.5})$$

2 Spherical Bessel function

The Bessel function $j_l(x)$ is defined by the following differential equation:

$$\frac{d^2 j_l}{dx^2} + \frac{2}{x} \frac{dj_l}{dx} + \left[1 - \frac{l(l+1)}{x^2}\right] j_l = 0 \quad (\text{C.6})$$

in which:

$$j_0(x) = \frac{\sin(x)}{x} \quad (\text{C.7})$$

$$j_1(x) = \frac{\sin(x) - x \cos(x)}{x^2} \quad (\text{C.8})$$

It satisfies the following relation:

$$\frac{dj_l}{dx} = j_{l-1} - \frac{l+1}{x} j_l \quad (\text{C.9})$$

It is related to the Legendre polynomial function by:

$$\frac{1}{2} \int_{-1}^1 d\mu \mathcal{L}_l(\mu) \exp(ix\mu) = \frac{j_l(x)}{(-i)^l} \quad (\text{C.10})$$

$$\exp(j\vec{k}\vec{x}) = \sum_{l=0}^{\infty} j^l (2l+1) j_l(kx) \mathcal{L}_l(\hat{k}\hat{x}) \quad (\text{C.11})$$

3 Fourier tranforms

The Fourier transform is defined by:

$$F(\vec{x}) = \int \frac{d^3k}{(2\pi)^3} \exp(i\vec{k}\vec{x}) f(\vec{k}) \quad (\text{C.12})$$

$$f(\vec{k}) = \int d^3x \exp(-i\vec{k}\vec{x}) F(\vec{x}) \quad (\text{C.13})$$

Bibliography

- [1] R. Maartens, F. B. Abdalla, M. Jarvis and M. G. Santos, *Overview of Cosmology with the SKA*, *PoS AASKA14* (2015) 016 [[1501.04076](#)].
- [2] C. A. P. Bengaly, R. Maartens and M. G. Santos, *Probing the Cosmological Principle in the counts of radio galaxies at different frequencies*, *JCAP* **1804** (2018) 031 [[1710.08804](#)].
- [3] J. Ripa and A. Shafieloo, *Testing the Isotropic Universe Using the Gamma-Ray Burst Data of Fermi/GBM*, *Astrophys. J.* **851** (2017) 15 [[1706.03556](#)].
- [4] Y. Y. Wang and F. Y. Wang, *Testing the isotropy of the Universe with type Ia supernovae in a model-independent way*, *Mon. Not. Roy. Astron. Soc.* **474** (2018) 3516 [[1711.05974](#)].
- [5] J. J. Condon, W. D. Cotton, E. W. Greisen, Q. F. Yin, R. A. Perley, G. B. Taylor et al., *The NRAO VLA Sky survey*, *Astron. J.* **115** (1998) 1693.
- [6] Chris J. Salter, Robert L. Brown, *Galactic and Extragalactic Radio Astronomy*, Astronomy and Astrophysics Library. Springer-Verlag New York, 2 ed., 1988.
- [7] A. Saxena, M. Marinello, R. A. Overzier, P. N. Best, H. J. A. Röttgering, K. J. Duncan et al., *Discovery of a radio galaxy at $z = 5.72$* , *mnras* **480** (2018) [[1806.01191](#)].
- [8] J. Condon, *An Analysis of the VLASS Proposal*, [1502.05616](#).
- [9] M. J. Jarvis et al., *A JVLA 10 degree² deep survey*, [1401.4018](#).
- [10] M. P. Hobson, G. P. Efstathiou and A. N. Lasenby, *General relativity: an introduction for physicists*. Cambridge University Press, 2006.
- [11] D. Saadeh, S. M. Feeney, A. Pontzen, H. V. Peiris and J. D. McEwen, *How isotropic is the Universe?*, *Phys. Rev. Lett.* **117** (2016) 131302 [[1605.07178](#)].
- [12] C. Clarkson, *Establishing homogeneity of the universe in the shadow of dark energy*, *Comptes Rendus Physique* **13** (2012) 682 [[1204.5505](#)].
- [13] D. Baumann, *Inflation*, [0907.5424](#).
- [14] C. Knebel, *An introduction into the theory of cosmological structure formation*, [1208.5931](#).
- [15] J. Bagchi, S. Sankhyayan, P. Sarkar, S. Raychaudhury, J. Jacob and P. Dabhade, *Saraswati: An Extremely Massive 200 Megaparsec Scale Supercluster*, *Astrophys. J.* **844** (2017) 25 [[1707.03082](#)].

- [16] *S. D. Csaba Csaki*, Physics of the Large and the Small: Tasi 2009, Proceedings of the 2009 Theoretical Advanced Study Institute in Elementary Particle Physics. *World Scientific Publishing Company*, 2011.
- [17] *M. Rubart and D. J. Schwarz*, Cosmic radio dipole from NVSS and WENSS, *Astron. Astrophys.* **555** (2013) A117 [[1301.5559](#)].
- [18] *K. M. Gorski, B. D. Wandelt, F. K. Hansen, E. Hivon and A. J. Banday*, The healpix primer, [astro-ph/9905275](#).
- [19] *K. M. Gorski, E. Hivon, A. J. Banday, B. D. Wandelt, F. K. Hansen, M. Reinecke et al.*, HEALPix - A Framework for high resolution discretization, and fast analysis of data distributed on the sphere, *Astrophys. J.* **622** (2005) 759 [[astro-ph/0409513](#)].
- [20] *H. S. Xavier, F. B. Abdalla and B. Joachimi*, Improving lognormal models for cosmological fields, *Mon. Not. Roy. Astron. Soc.* **459** (2016) 3693 [[1602.08503](#)].
- [21] *H. S. Xavier, F. B. Abdalla and B. Joachimi*, Flask: Full-sky lognormal astro-fields simulation kit, *Astrophysics Source Code Library* (2016) .
- [22] *J. J. Condon, W. D. Cotton, E. W. Greisen, Q. F. Yin, R. A. Perley, G. B. Taylor et al.*, The NRAO VLA Sky survey, *Astron. J.* **115** (1998) 1693.
- [23] *H. S. Xavier, F. B. Abdalla and B. Joachimi*, Improving lognormal models for cosmological fields, *Mon. Not. Roy. Astron. Soc.* **459** (2016) 3693 [[1602.08503](#)].
- [24] *A. Challinor and A. Lewis*, The linear power spectrum of observed source number counts, *Phys. Rev.* **D84** (2011) 043516 [[1105.5292](#)].
- [25] *R. J. Wilman et al.*, A semi-empirical simulation of the extragalactic radio continuum sky for next generation radio telescopes, *Mon. Not. Roy. Astron. Soc.* **388** (2008) 1335 [[0805.3413](#)].
- [26] *PLANCK collaboration, P. A. R. Ade et al.*, Planck 2015 results. XXI. The integrated Sachs-Wolfe effect, *Astron. Astrophys.* **594** (2016) A21 [[1502.01595](#)].
- [27] *L. B. W. Frederick J Gravetter*, Statistics for the Behavioral Sciences. *Wadsworth Publishing*, 9 ed., 2012.